canonical ADAMs (Supplementary Figure 1). Comparison of the recently solved ADAM10 D/C-domain partial structure ($ADAM10_{D+C}$) (Janes *et al*, 2005) and that of VAP1 reveals that the atypical ADAM10 shares the continuous D_a/C_w structure and the C_h-domain scaffold with VAP1; however, it has an disordered D_s-domain and an alternate HVR structure and a different orientation between C_w- and C_h-domains (Figure 6). The locations of four of the five disulfide bridges within the C_h-domain are conserved between VAP1 and ADAM10 (Figure 6B and C) and thus, they enabled us to align the two sequences (Figure 6E). Based on this alignment, we completed entire alignments (Supplementary Figure 1) including 38 sequences of mammalian ADAMs and *Schizosaccharomyces pombe* Mde10 (Nakamura *et al*, 2004), presumably the founding member of the ADAM family in evolutionary terms. The $ADAM10_{D+C}$ structure lacks the eight residues (583–590 in ADAM10) that may form a flexible loop. However, VAP1 (Figure 6E) and the canonical ADAMs except for ADAM8 (Supplementary Figure 1) have extra 16 residues in this segment that, in part, forms a variable loop, flanked by the adjacent cysteinyl residues (Cys539 and Cys549 in VAP1) and protrudes from the main body of the C-domain (Figures 4A and 6B). The variable loop has highest temperature factor in the molecule and resembles to the disintegrin-loop, thus can be an additional protein-binding interface. The six VAP1 monomer molecules represent almost the same C_w/C_h domain orientation (data not shown), however that is distinct from that of ADAM10 (Figure 5A). Thus, the possibility whether different ADAMs have distinct C_w/C_h domain orientation remains to be established. Janes *et al* (2005) have shown that the three glutamate residues outside of HVR are essential for ADAM10-mediated ephrin proteolysis in *trans*, however, roles of the ADAM10 HVR has not been examined. An extensive molecular surface of the elongated arm structure (12 000 Å^2 for the VAP1 D/C-domains) might reveal additional protein–protein interaction interfaces other than the HVR. Multiple charged residues in the D-domain are essential for ADAM28 binding to α4β1 (Bridges *et al*, 2003) and the RX_6DLPEF motif has been proposed for integrin α9β1 binding (Eto *et al*, 2002). However, the D-domain portion of the C-shaped scaffold is away from the catalytic site; thus, those additional sites might not directly serve as target recognition interfaces for catalysis.

Uniquely among cell-surface proteins, ADAMs display both proteolytic and adhesive activities. The VAP1 structure reveals that these functions are spatially allocated to the ends of the unique C-shaped scaffold and face each other. This spatial allocation of the functional sites provide us insights

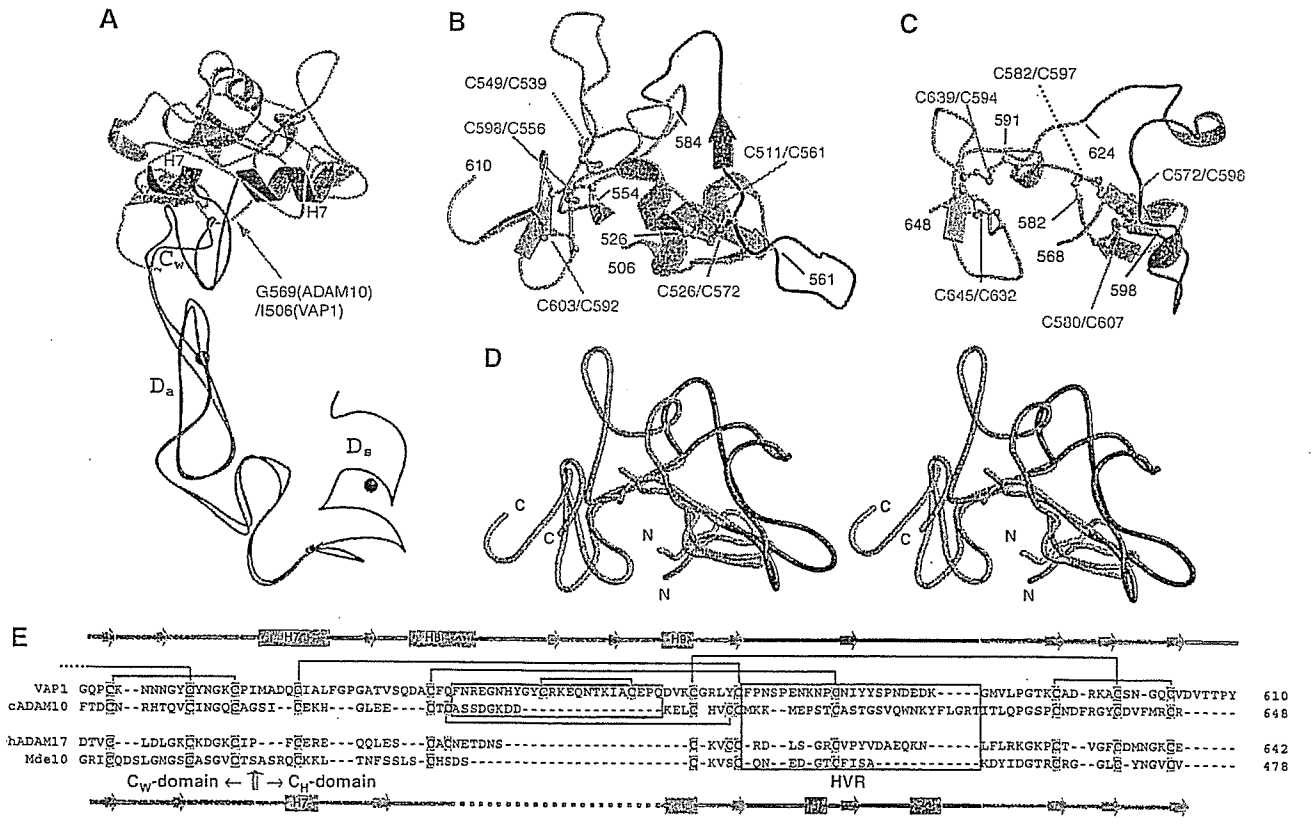

Figure 6 Comparison of the VAP1 and ADAM10 D/C domains. (A) Superimposition of the D_a-domains of ADAM10 and VAP1. The $D_s/D_a/C_w$-domains and the H7 helix of VAP1 and those of ADAM10 are shown in blue and red, respectively. The C_h-domains of VAP1 and ADAM10 are shown in cyan and pink, respectively. The arrow indicates the pivotal point between the C_w- and C_h-domains. Bound Ca^{2+} ions in VAP1 are shown as black spheres. (B) Ribbon representation of the C_h-domain of VAP1. The HVR is shown in blue. The common scaffold between the VAP1 and ADAM10 C_h-domains are shown in cyan and the segment lacking in ADAM10 is shown in light green. Disulfide bridges are indicated. (C) Ribbon representation of the C_h-domain of ADAM10. The HVR is shown in red. Disulfide brides are indicated. (D) Superimposition of the C_h-domains of VAP1 and ADAM10 *in stereo* with the colors as in (B, C). The N- and C-termini of the C_h-domains are indicated. (E) Structure-based alignments of VAP1, bovine ADAM10 (cADAM10), human ADAM17 (hADAM17) and *S. pombe* Mde10 (Mde10) C_w/C_h-domains. Secondary structures and the disulfide bridges are represented schematically. The HVR sequences and the missing segment in the ADAM10 structure are boxed in blue and green, respectively.

into the molecular mechanism of ADAMs' target recognition, which ADAMs shed which key substrates in specific biological events. Since ADAMs are potential therapeutic targets, the distinct surface feature created by the HVR of the individual ADAMs might also provide insights into the future design of drugs with higher specificity for each member of ADAMs. We suggest that the HVR, not the disintegrin domain, should be the focus of searches for physiological targets of ADAMs.

Materials and methods

Protein preparation and crystallization

The details of the preparation, crystallization and preliminary X-ray analysis of VAP1 will be described elsewhere (T Igarashi *et al*, in preparation). VAP1 was isolated from the crude snake *Crotalus atrox* venom (Sigma-Aldrich, USA) and subjected to sitting- or hanging-drop vapor diffusion crystallization. Two distinct crystal forms ($P2_12_12_1$ and $P4_12_12$) were obtained with the reservoir solution containing 15% polyethyleneglycol 8000 and 100 mM sodium cacodylate at pH 6.5, with (orthorhombic form) or without (tetragonal form) 20 mM cobaltous chloride hexahydrate. GM6001-bound crystals were prepared by adding GM6001 (CALBIOCHEM) to the drop with the orthorhombic crystal at a final concentration qof 0.33 mM (twice the protein concentration) followed by a 12-h incubation. Crystals were flash-frozen under the nitrogen flow at 90 K.

Diffraction data collection

All the diffraction data were collected at SPring-8 beamlines using either ADSC quantum 310R CCD (for the inhibitor-bound crystal at the beamline BL41XU with $\lambda = 1$ Å), Rigaku *R*-axis V imaging plate (for orthorhombic native crystal at the beamline BL45PX with $\lambda = 1$ Å) or Jupitor CCD (for the tetragonal crystal at the beamline BL45PX with $\lambda = 0.98$ Å) detectors at 90 K. The images were reduced using HKL2000. Both orthorhombic and tetragonal native data sets were collected to 2.5-Å resolution and inhibitor-bound crystal data sets were collected to 3.0 Å resolution (Table I).

Structural analysis

All structures were solved by the molecular replacement method by MOLREP in the CCP4 suite (CCP4, 1994) by using acutolysin-C (1QUA) (Zhu *et al*, 1999) as a starting model. Initially, the MR solution obtained from the orthorhombic crystal data set, assumed two M-domains in the asymmetric units. After manual rebuilding by TURBO-FRODO, the model was subjected to tortional molecular dynamic refinements with restrained NCS averaging of the M-domains using CNS (Brunger *et al*, 1998) and iterative refinements and manual rebuilding of the model improved the electron-density map and enabled us to extend the model. First, we found the electron densities associated with the pieces of helical segments of the molecules and modelled them as poly-alanine chains. After cycles of refinements, we assigned those segments as the parts of helices H7 and H8, where the secondary structures are predicted to be helices, judging from the electron densities associated with the side chains. At this stage, four tyrosine residues, Tyr575 and Try576 within the central β strands of the HVRs were clearly defined, and we noticed that there was another NCS-axis between the C-domains. After iterative rounds of refinements with restrained NCS averaging of the C-domains and manual model building, we completed modelling of the C-domains. From this stage onward, no NCS averaging was included in the refinements. Next, we modelled the D-domains with the help of automated chain tracing using the program ARP/wARP (Perrakis *et al*, 1999) and with the structural model of trimestatin (1J2L) as a guide. After completely modelling the polypeptide chains, we noticed that isolated lobes of high electron densities surrounded by oxygen atoms occurred both in the D_s- and D_a-domains. For these sites, calcium ions fit optimally to the electron density with a refined occupancy of 100% and reasonably low *B*-values, thus, we included calcium ions in the model. We also assigned a cobalt ion, which was supplemented in the crystallization buffer for the orthorhombic crystal form, located between the M- and D_s-domains in the A molecule. The part of the carbohydrate chain linked to residue Asn218 (two *N*-acetylglocosamine (NAG) moieties) was modelled. Then, water molecules were assigned. The *VAP1* cDNA encodes a protein with 610 amino-acid residues; however, the N-terminus is processed by post-translational modification (Masuda *et al*, 1998, 2000). Here, protein sequencing of the de-blocked VAP1 molecule clarified that the Glu184 side chain was modified into a pyro-form. The electron densities associated with almost the entire molecule except for the first pyroglutamic acid were defined in either monomer within the orthorhombic crystal. In the final model, 86.1% of the residues lay in the most favorable region, 13.3% in the additionally allowed region and 0.7% in the generously allowed region of the Ramachandran plot. The tetragonal crystal and inhibitor-bound crystal were solved by MR with the domains of the refined orthorhombic apo-form as a starting model. In the final model, 83.6% (80.6%) of the residues lay in the most favorable region, 15.7% (18.9%) in the additionally allowed region and 0.7% (0.5%) in the generously allowed region for tetragonal (inhibitor-bound) crystals in the Ramachandran plot. In either crystal form, the asymmetric unit contained one dimer molecule. All six monomers had almost identical structures. Refinement statistics are shown in Table I.

PDB accession codes

Atomic coordinates and structure factors have been deposited in the Protein Data Bank under accession codes 2ERO, 2ERP and 2ERQ for the orthorhombic native, GM6001-bound form and tetragonal-form, respectively.

Supplementary data

Supplementary data are available at *The EMBO Journal* Online.

Acknowledgements

We thank Yuko Oishi and staff in SPring-8 beamlines for assistance with data acquisition and Junichi Takagi for discussions and critical reading of the manuscript. This work was partly supported by Grant nano-001 for Research on Advanced Medical Technology from the Ministry of Health, Labor, and Welfare of Japan, and by grants from the Takeda Science Foundation, from the Kao Foundation for Arts and Science and from Senri Life Science Foundation. The authors declare no competing financial interests.

References

Almeida EA, Huovila AP, Sutherland AE, Stephens LE, Calarco PG, Shaw LM, Mercurio AM, Sonnenberg A, Primakoff P, Myles DG, White JM (1995) Mouse egg integrin alpha 6 beta 1 functions as a sperm receptor. *Cell* 81: 1095–1104

Becherer JD, Blobel CP (2003) Biochemical properties and functions of membrane-anchored metalloprotease-disintegrin proteins (ADAMs). *Curr Top Dev Biol* 54: 101–123

Black RA, Rauch CT, Kozlosky CJ, Peschon JJ, Slack JL, Wolfson MF, Castner BJ, Stocking KL, Reddy P, Srinivasan S, Nelson N, Boiani N, Schooley KA, Gerhart M, Davis R, Fitzner JN, Johnson RS, Paxton RJ, March CJ, Cerretti DP (1997) A metalloproteinase disintegrin that releases tumour-necrosis factor-alpha from cells. *Nature* 385: 729–733

Blobel CP (2005) ADAMs: key components in EGFR signalling and development. *Nat Rev Mol Cell Biol* 6: 32–43

Blobel CP, Myles DG, Primakoff P, White JM (1990) Proteolytic processing of a protein involved in sperm-egg fusion correlates with acquisition of fertilization competence. *J Cell Biol* 111: 69–78

Blobel CP, Wolfsberg TG, Turck CW, Myles DG, Primakoff P, White JM (1992) A potential fusion peptide and an integrin ligand domain in a protein active in sperm-egg fusion. *Nature* 356: 248–252

Bode W, Gomis-Ruth FX, Stockler W (1993) Astacins, serralysins, snake venom and matrix metalloproteinases exhibit identical zinc-binding environments (HEXXHXXGXXH and Met-turn) and

topologies and should be grouped into a common family, the 'metzincins'. *FEBS Lett* 331: 134–140

Bridges LC, Hanson KR, Tani PH, Mather T, Bowditch RD (2003) Integrin alpha4beta1-dependent adhesion to ADAM 28 (MDC-L) requires an extended surface of the disintegrin domain. *Biochemistry* 42: 3734–3741

Brunger AT, Adams PD, Clore GM, DeLano WL, Gros P, Grosse-Kunstleve RW, Jiang JS, Kuszewski J, Nilges M, Pannu NS, Read RJ, Rice LM, Simonson T, Warren GL (1998) Crystallography & NMR system: a new software suite for macromolecular structure determination. *Acta Crystallogr D* 54 (Part 5): 905–921

Calvete JJ, Marcinkiewicz C, Monleon D, Esteve V, Celda B, Juarez P, Sanz L (2005) Snake venom disintegrins: evolution of structure and function. *Toxicon* 45: 1063–1074

CCP4 (1994) The CCP4 suite: programs for protein crystallography. *Acta Crystallogr D* 50: 760–763

Duffy MJ, Lynn DJ, Lloyd AT, O'Shea CM (2003) The ADAMs family of proteins: from basic studies to potential clinical applications. *Thromb Haemost* 89: 622–631

Eto K, Huet C, Tarui T, Kupriyanov S, Liu HZ, Puzon-McLaughlin W, Zhang XP, Sheppard D, Engvall E, Takada Y (2002) Functional classification of ADAMs based on a conserved motif for binding to integrin alpha 9beta 1: implications for sperm-egg binding and other cell interactions. *J Biol Chem* 277: 17804–17810

Evans JP (2001) Fertilin beta and other ADAMs as integrin ligands: insights into cell adhesion and fertilization. *BioEssays* 23: 628–639

Fox JW, Serrano SM (2005) Structural considerations of the snake venom metalloproteinases, key members of the M12 reprolysin family of metalloproteinases. *Toxicon* 45: 969–985

Fujii Y, Okuda D, Fujimoto Z, Horii K, Morita T, Mizuno H (2003) Crystal structure of trimestatin, a disintegrin containing a cell adhesion recognition motif RGD. *J Mol Biol* 332: 1115–1122

Gaultier A, Cousin H, Darribere T, Alfandari D (2002) ADAM13 disintegrin and cysteine-rich domains bind to the second heparin-binding domain of fibronectin. *J Biol Chem* 277: 23336–23344

Huang TF, Holt JC, Lukasiewicz H, Niewiarowski S (1987) Trigramin. A low molecular weight peptide inhibiting fibrinogen interaction with platelet receptors expressed on glycoprotein IIb–IIIa complex. *J Biol Chem* 262: 16157–16163

Iba K, Albrechtsen R, Gilpin B, Frohlich C, Loechel F, Zolkiewska A, Ishiguro K, Kojima T, Liu W, Langford JK, Sanderson RD, Brakebusch C, Fassler R, Wewer UM (2000) The cysteine-rich domain of human ADAM 12 supports cell adhesion through syndecans and triggers signaling events that lead to beta1 integrin-dependent cell spreading. *J Cell Biol* 149: 1143–1156

Janes PW, Saha N, Barton WA, Kolev MV, Wimmer-Kleikamp SH, Nievergall E, Blobel CP, Himanen JP, Lackmann M, Nikolov DB (2005) Adam meets Eph: an ADAM substrate recognition module acts as a molecular SWITCH for Ephrin cleavage *in trans*. *Cell* 123: 291–304

Jia LG, Shimokawa K, Bjarnason JB, Fox JW (1996) Snake venom metalloproteinases: structure, function and relationship to the ADAMs family of proteins. *Toxicon* 34: 1269–1276

Jia LG, Wang XM, Shannon JD, Bjarnason JB, Fox JW (2000) Inhibition of platelet aggregation by the recombinant cysteine-rich domain of the hemorrhagic snake venom metalloproteinase, atrolysin A. *Arch Biochem Biophys* 373: 281–286

Kamiguti AS, Gallagher P, Marcinkiewicz C, Theakston RD, Zuzel M, Fox JW (2003) Identification of sites in the cysteine-rich domain of the class P-III snake venom metalloproteinases responsible for inhibition of platelet function. *FEBS Lett* 549: 129–134

Maskos K, Fernandez-Catalan C, Huber R, Bourenkov GP, Bartunik H, Ellestad GA, Reddy P, Wolfson MF, Rauch CT, Castner BJ, Davis R, Clarke HR, Petersen M, Fitzner JN, Cerretti DP, March CJ, Paxton RJ, Black RA, Bode W (1998) Crystal structure of the catalytic domain of human tumor necrosis factor-alpha-converting enzyme. *Proc Natl Acad Sci USA* 95: 3408–3412

Masuda S, Hayashi H, Araki S (1998) Two vascular apoptosis-inducing proteins from snake venom are members of the metalloprotease/disintegrin family. *Eur J Biochem* 253: 36–41

Masuda S, Ohta T, Kaji K, Fox JW, Hayashi H, Araki S (2000) cDNA cloning and characterization of vascular apoptosis-inducing protein 1. *Biochem Biophys Res Commun* 278: 197–204

Moss ML, Bartsch JW (2004) Therapeutic benefits from targeting of ADAM family members. *Biochemistry* 43: 7227–7235

Moss ML, Jin SL, Milla ME, Bickett DM, Burkhart W, Carter HL, Chen WJ, Clay WC, Didsbury JR, Hassler D, Hoffman CR, Kost TA, Lambert MH, Leesnitzer MA, McCauley P, McGeehan G, Mitchell J, Moyer M, Pahel G, Rocque W, Overton LK, Schoenen F, Seaton T, Su JL, Warner J, Willard D, Becherer JD (1997) Cloning of a disintegrin metalloproteinase that processes precursor tumour-necrosis factor-alpha. *Nature* 385: 733–736

Myles DG, Kimmel LH, Blobel CP, White JM, Primakoff P (1994) Identification of a binding site in the disintegrin domain of fertilin required for sperm-egg fusion. *Proc Natl Acad Sci USA* 91: 4195–4198

Nakamura T, Abe H, Hirata A, Shimoda C (2004) ADAM family protein Mde10 is essential for development of spore envelopes in the fission yeast *Schizosaccharomyces pombe*. *Eukaryot Cell* 3: 27–39

Orth P, Reichert P, Wang W, Prosise WW, Yarosh-Tomaine T, Hammond G, Ingram RN, Xiao L, Mirza UA, Zou J, Strickland C, Taremi SS, Le HV, Madison V (2004) Crystal structure of the catalytic domain of human ADAM33. *J Mol Biol* 335: 129–137

Pan D, Rubin GM (1997) Kuzbanian controls proteolytic processing of Notch and mediates lateral inhibition during *Drosophila* and vertebrate neurogenesis. *Cell* 90: 271–280

Perrakis A, Morris R, Lamzin VS (1999) Automated protein model building combined with iterative structure refinement. *Nat Struct Biol* 6: 458–463

Primakoff P, Hyatt H, Tredick-Kline J (1987) Identification and purification of a sperm surface protein with a potential role in sperm-egg membrane fusion. *J Cell Biol* 104: 141–149

Qi H, Rand MD, Wu X, Sestan N, Wang W, Rakic P, Xu T, Artavanis-Tsakonas S (1999) Processing of the notch ligand delta by the metalloprotease Kuzbanian. *Science* 283: 91–94

Reddy P, Slack JL, Davis R, Cerretti DP, Kozlosky CJ, Blanton RA, Shows D, Peschon JJ, Black RA (2000) Functional analysis of the domain structure of tumor necrosis factor-alpha converting enzyme. *J Biol Chem* 275: 14608–14614

Rooke J, Pan D, Xu T, Rubin GM (1996) KUZ, a conserved metalloprotease-disintegrin protein with two roles in *Drosophila* neurogenesis. *Science* 273: 1227–1231

Seals DF, Courtneidge SA (2003) The ADAMs family of metalloproteases: multidomain proteins with multiple functions. *Genes Dev* 17: 7–30

Serrano SM, Jia LG, Wang D, Shannon JD, Fox JW (2005) Function of the cysteine-rich domain of the haemorrhagic metalloproteinase atrolysin A: targeting adhesion proteins collagen I and von Willebrand factor. *Biochem J* 391: 69–76

Smith KM, Gaultier A, Cousin H, Alfandari D, White JM, DeSimone DW (2002) The cysteine-rich domain regulates ADAM protease function *in vivo*. *J Cell Biol* 159: 893–902

Van Eerdewegh P, Little RD, Dupuis J, Del Mastro RG, Falls K, Simon J, Torrey D, Pandit S, McKenny J, Braunschweiger K, Walsh A, Liu Z, Hayward B, Folz C, Manning SP, Bawa A, Saracino L, Thackston M, Benchekroun Y, Capparell N, Wang M, Adair R, Feng Y, Dubois J, FitzGerald MG, Huang H, Gibson R, Allen KM, Pedan A, Danzig MR, Umland SP, Egan RW, Cuss FM, Rorke S, Clough JB, Holloway JW, Holgate ST, Keith TP (2002) Association of the ADAM33 gene with asthma and bronchial hyperresponsiveness. *Nature* 418: 426–430

White JM (2003) ADAMs: modulators of cell–cell and cell–matrix interactions. *Curr Opin Cell Biol* 15: 598–606

Yagami-Hiromasa T, Sato T, Kurisaki T, Kamijo K, Nabeshima Y, Fujisawa-Sehara A (1995) A metalloprotease-disintegrin participating in myoblast fusion. *Nature* 377: 652–656

Zhu X, Teng M, Niu L (1999) Structure of acutolysin-C, a haemorrhagic toxin from the venom of Agkistrodon acutus, providing further evidence for the mechanism of the pH-dependent proteolytic reaction of zinc metalloproteinases. *Acta Crystallogr D* 55: 1834–1841

Zolkiewska A (1999) Disintegrin-like/cysteine-rich region of ADAM 12 is an active cell adhesion domain. *Exp Cell Res* 252: 423–431

Summary: An amphiphilic poly(*N*-propargylamide) with galactose and lauryloyl groups was synthesized by copolymerization of the corresponding *N*-propargylamide monomers using a Rh catalyst. The obtained copolymer formed a one-handed helical conformation and molecular aggregates in water. The observations by fluorescence microscopy in a cell culture experiment in the presence of dye-labeled copolymer indicated that the copolymer was incorporated into the cells.

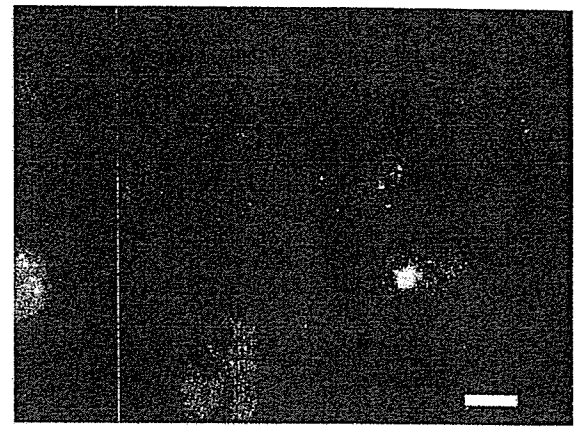

Localization of rhodamine B-labeled copolymer **8** in human aortic endothelial cells (fluorescence image).

Amphiphilic Poly(*N*-propargylamide) with Galactose and Lauryloyl Groups: Synthesis and Properties

Masakaza Suenaga,[1] *Yoshiro Kaneko,*[1] *Jun-ichi Kadokawa,**[1] *Takehiro Nishikawa,*[2] *Hideyo Mori,*[2] *Masayoshi Tabata*[3]

[1]Department of Nanostructured and Advanced Materials, Graduate School of Science and Engineering, Kagoshima 890-0065, Japan
Fax: +81-99-285-3253; E-mail: kadokawa@eng.kagoshima-u.ac.jp
[2]National Cardiovascular Center, Suita, Osaka 565-8565, Japan
[3]Department of Molecular Chemistry, Graduate School of Engineering, Hokkaido University, Sapporo 060-8628, Japan

Received: July 19, 2006; Accepted: October 10, 2006; DOI: 10.1002/mabi.200600228

Keywords: amphiphiles; conjugated polymers; copolymerization; dynamic light scattering; nanoparticles; polyacetylenes

Introduction

Synthesis of polymers having sugar residues, so-called glycopolymers, has been widely investigated to seek biological applications because of their versatile functions.[1] It has been demonstrated that these glycopolymers can bind specifically to carbohydrate-recognition proteins, toxins, viruses, and cells, and, thus, these polymers can be utilized as cell culture substrates with specific cell recognition sites, as well as in targeting drug delivery systems.[2] The clustered saccharide ligands conjugated to the polymeric main chains are involved in these specific recognition processes. Most of the previously prepared glycopolymers have been based on a flexible polymer backbone, such as polystyrene and polyacrylamide.[3,4] This flexible nature of the glycopolymers causes the disordered orientation of the sugar residues in the glycopolymers. Regular orientation of the sugar residues is necessary for efficient interaction between the glycopolymers and receptor molecules. In this sense, the spatially regulated orientation of the sugar residues should be realized by attaching the sugar residues to a polymer backbone with a rigid conformation. The sugar residues attached to the rigid polymer backbone may give rise to the ordered orientation that can improve the molecular recognition of sugar residues by specific cell receptors. This is because the spatial regulation of the sugar residues is significant in molecular recognition as well as the chemical structure of the sugar molecules.[5]

From the above viewpoints, rigid glycopolymers with π-conjugated polymer backbones would be a novel type of bio-inspired polymers, which could exhibit multiple valence states and interact specifically and firmly with targets such as cell surface receptors and biomacromolecules. In some previous works, rigid glycopolymers having various π-conjugated main chains, such as polythiophene,[6] poly(*p*-phenylene ethynylene),[7] polyisocyanide,[8] polyaniline,[9] poly(*p*-phenylene vinylene),[10] and poly(phenylacetylene), have already been synthesized.[11] In the series of these studies, we reported the synthesis of poly(*N*-propargylamide) (**2**) with sugar residues. It contained a *cis*-polyacetylene main chain and was obtained by the rhodium-catalyzed polymerization of a *N*-propargylamide monomer (**1**) that had a galactose residue (Scheme 1).[12] Since polymerizations of the *N*-propargylamide monomers having various substituted groups using Rh catalyst have been widely reported to produce the corresponding poly(*N*-propargylamide) derivatives with *cis*-isomers,[13] we also investigated the copolymerization of **1** with *N*-propargylamide derivative **3** having a hexanoyl group to produce the amphiphilic glycopolymer **4**, as shown in Scheme 1. We tested the solubility of copolymer **4** in various solvents to confirm whether the copolymer exhibits an amphiphilic property. Although the homopolymer **2** is insoluble in common organic solvents, the copolymer **4** can be dissolved in some polar organic solvents, such as dimethyl sulfoxide (DMSO) and *N,N*-dimethylformamide (DMF), as well as in aqueous medium. However, the copolymer still exhibits a hydrophilic nature rather than an amphiphilic nature. We assumed that insufficient amphiphilicity of copolymer **4** could be attributed to poor hydrophobic property of the hydrophobic part.

In this study, we chose a more hydrophobic monomer: *N*-propargylamide monomer **5** having a longer alkyl chain, i.e., the lauryloyl group, as the hydrophobic part of the amphiphilic copolymer. The monomer **5** was copolymerized with **1** in the presence of Rh catalyst to give the corresponding amphiphilic copolymer **6** (Scheme 2). The resulting copolymer **6** can be expected to have the ability to conduct molecular aggregation in water, which is driven by intermolecular and intramolecular association of the hydrophobic lauryloyl groups.

We believe that such molecular aggregates of the amphiphilic copolymer should play a significant role in the field of targeted drug delivery. The idea is supported by the following characteristics of the molecular aggregates:

1) Drug carriers with nanometer dimensions can be obtained by molecular aggregation of amphiphilic copolymers.
2) Nano-sized aggregates can remain in the bloodstream for an extended period because of the size-dependent uptake in the reticuloendothelial system.
3) Drug molecules with hydrophobic natures can be loaded into hydrophobic milieus formed by the association of hydrophobic long alkyl chains; otherwise the drug molecules could be directly attached to the constituent monomer molecules of the copolymer.
4) Sugar residues of the copolymer can function as recognition sites for target cells and tissues as well as providing the hydrophilic character of the amphiphilic copolymer.

Therefore, we studied the *in vitro* cell uptake of the molecular aggregates of the amphiphilic copolymer. For this purpose, the fluorescent marker, rhodamine B, was introduced into the amphiphilic copolymer. In this article, we report the synthesis of the amphiphilic

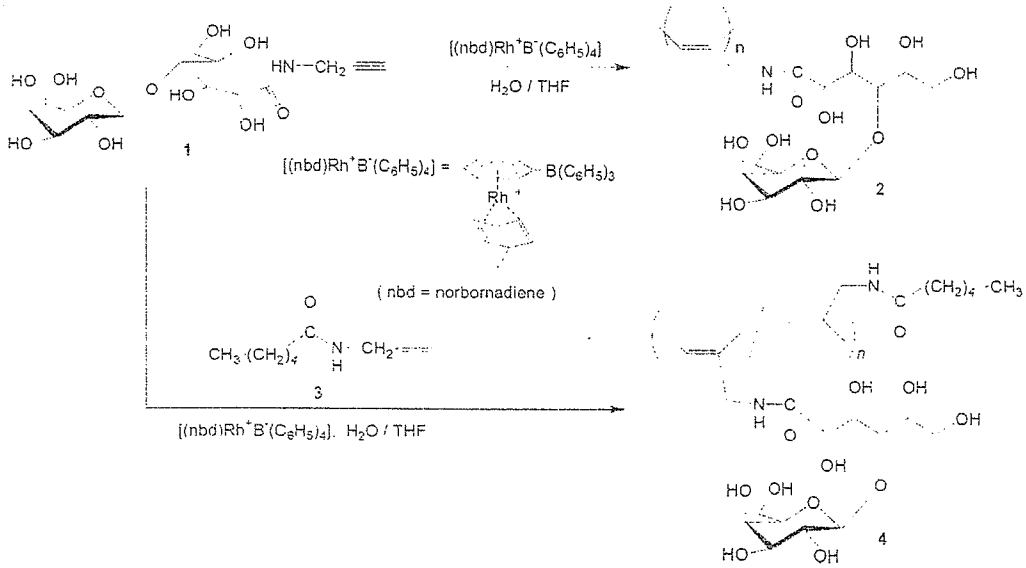

Scheme 1. Polymerization of **1** and copolymerization of **1** with **3**.

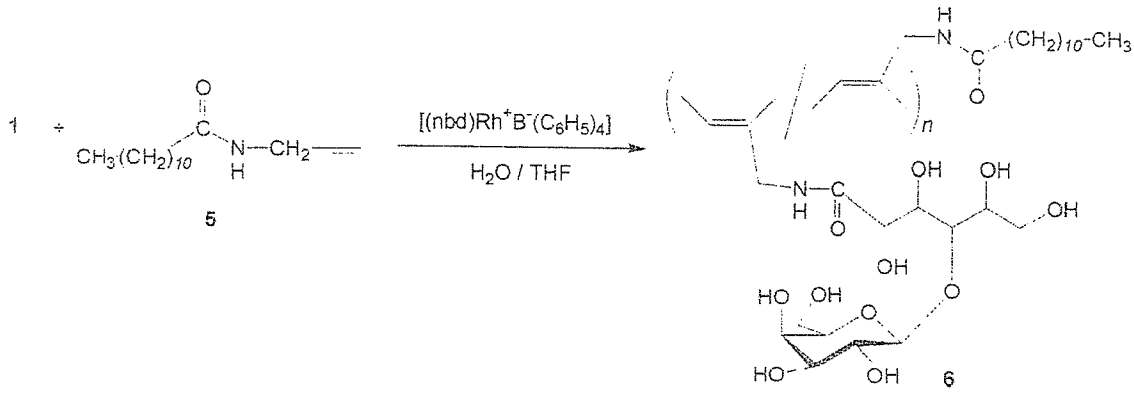

Scheme 2. Copolymerization of 1 with 5.

poly(*N*-propargylamide) **6** by Rh-catalyzed copolymerization, evaluation of its molecular aggregation in water [gel permeation chromatography (GPC) characterization, scanning electron microscopy (SEM) observation, and dynamic light scattering (DLS) measurement] and secondary conformation [circular dichroism (CD) spectra], and cell uptake of the nanoaggregate of the rhodamine-labeled amphiphilic copolymer (fluorescence microscopy).

Experimental Part

Materials

Monomer **1** and catalyst (nbd)Rh$^+$B$^-$(C_6H_5)$_4$ were prepared according to the literature.[12,14] Tetrahydrofuran (THF) used as polymerization solvent was purified by distillation. Other reagents and solvents were used as received without further purification.

Synthesis of Monomer 5

Monomer **5** was synthesized by a method similar to that used for **3**.[15] Under argon, *N*-propargylamine hydrochloride (0.915 g, 10.0 mmol) was dissolved by slight warming in anhydrous acetonitrile (12.0 mL), and triethylamine (3.35 mL, 24.0 mmol) was added to the solution at room temperature. Then a solution of lauryloyl chloride (2.36 mL, 10.0 mmol) in anhydrous acetonitrile (12.0 mL) was added dropwise to the solution. After the mixture was stirred for 2 h, the reaction solution was concentrated by evaporation. The residue was dissolved in ethyl acetate and the solution was washed successively three times with 2 mol·L^{-1} hydrochloric acid and with saturated $NaHCO_3$ aqueous solution. The organic layer was dried over anhydrous Na_2SO_4, filtered, and evaporated. The residue was subjected to column chromatography on silica gel (hexane:ethyl acetate = 4:1, v/v) to isolate **5** (1.38 g, 5.82 mmol) in 58.2% yield.

^{1}H NMR ($CDCl_3$): $\delta = 0.88$ (t, $J = 7.2$ Hz, CH_3, 3H), 1.28 [m, $CH_3(CH_2)_8$, 16H], 1.62 (m, $CH_2CH_2C{=}O$, 2H), 2.19 (t, $J = 7.8$ Hz, $CH_2C{=}O$, 2H), 2.23 (t, $J = 2.4$ Hz, H–C≡C, 1H), 4.05–4.06 (m, CH_2N, 2H), 5.57 (s, NH, 1H).

Synthesis of Monomer 7

Under argon, triethylamine (0.836 mL, 6.00 mmol) was added to a solution of *N*-propargylamine hydrochloride (0.549 g, 6.00 mmol) and rhodamine B (1.92 g, 4.0 mmol) in anhydrous methanol (10.0 mL) at 0 °C. To the solution was added 1-[(3-dimethylamino)propyl]-3-ethylcarbodiimide hydrochloride (1.15 g, 6.00 mmol) as a condensing agent at 0 °C and the mixture was stirred for 17 h at room temperature. The precipitated material was isolated by filtration and dried under the reduced pressure to give **7** (0.472 g, 0.915 mmol) in 23.0% yield.

^{1}H NMR ($CDCl_3$): $\delta = 1.16$ (m, CH_3, 12H), 1.77 (t, $J = 2.4$ Hz, H–C≡C, 1H), 3.33 (m, NCH_2CH_3, 8H), 3.95 (d, $J = 1.8$ Hz, $CH_2C{\equiv}$, 2H), 6.26–7.93 (m, aromatics, 10H).

Copolymerization of 1 with 5

A typical copolymerization procedure was as follows (entry 1, Table 1). Under argon, a solution of **5** (0.0356 g, 0.150 mmol) in THF (0.90 mL) and a solution of catalyst (0.00630 g, 0.0125 mmol) in THF (0.90 mL) were added to a solution of **1** (0.0397 g, 0.100 mmol) in water (0.20 mL) in this order at 30 °C. After the mixture was stirred at 30 °C for 140 min, the reaction mixture was concentrated by evaporation and dried under reduced pressure. The residue was dissolved in a small amount of DMSO and the solution was poured into a large amount of methanol to precipitate the polymeric product. The precipitate was isolated by filtration and was dried under reduced pressure to give **6** (0.0588 g) in 78.1% yield.

^{1}H NMR (DMSO-d_6): $\delta = 0.84$ (CH_3), 1.21 [$CH_3(CH_2)_8$], 1.45 ($CH_2CH_2C{=}O$), 2.15 ($CH_2C{=}O$), 3.0–3.9 [–CH(O–D-gal)–CH(OH)–CH_2OH, =CCH_2–, H2–H6 of D-gal], 4.04 [C(=O)CH(OH)CH(OH)–], 4.29 [C(=O)CH(OH)– and H1(β) of D-gal], 4.55, 4.79, 5.22 (OH), 6.11 (–CH=C–), 7.93 (NH).

Copolymerization of 1, 5, and 7

Under argon, a solution of **5** (0.0285 g, 0.120 mmol) and **7** (0.0929 g, 0.180 mmol) in THF (0.90 mL) and a solution of catalyst (0.0166 g, 0.0330 mmol) in THF (0.90 mL) were

Table 1. Results for copolymerization of **1** with **5** with Rh catalyst in THF–water (9:1) solvent.

Entry	Feed ratio[a]	Time	Yield[b]	Unit ratio[c]	$\overline{M}_n$[d]	$\overline{M}_w/\overline{M}_n$[d]	$[\alpha]_D$[e]
	1:**5**	min	%	**1**:**5**			degrees
1	1.0:1.5	140	78.1	1.0:0.92	9 100	1.30	-
2	1.0:1.0	195	62.5	1.0:0.88	6 200	1.63	-
3	1.0:0.67	240	57.0	1.0:0.35	5 200	1.60	-96.8
4	1.0:0.50	260	68.9	1.0:0.32	9 600	1.64	142.3
5	1.0:0.33	200	69.9	1.0:0.26	7 100	1.50	173.6
6	1.0:0.20	210	78.1	1.0:0.17	9 700	1.30	-185.6

[a] [Catalyst]/[**1** + **5**] = 0.05, reaction temperature: 30 °C.
[b] Fraction insoluble in methanol.
[c] Determined from ^{1}H NMR spectra.
[d] Determined by GPC with water as eluent using pullulan standards, sample concentration = 0.1 mg·mL^{-1}.
[e] Measured by polarimetry in water, c = 1.0 g·dL^{-1} at 20 °C.

added to a solution of **1** (0.143 g, 0.360 mmol) in water (0.20 mL) in this order at 30 °C. After the mixture was stirred at 30 °C for 18 h, the reaction mixture was concentrated by evaporation and dried under reduced pressure. The residue was dissolved in a small amount of DMSO and the solution was poured into a large amount of methanol to precipitate the polymeric product. The precipitate was isolated by filtration and dried under reduced pressure to give **8** (0.164 g) in 62.0% yield.

^{1}H NMR (DMSO-d_6 + D_2O): δ = 0.93 ($CH_3CH_2CH_2$), 1.16 (CH_3CH_2N), 1.25 [$CH_3(CH_2)_8$], 1.50 ($CH_2CH_2C{=}O$), 3.0–4.5 (sugar protons and =C–CH_2), 6.16 (HC=), 7.0–8.0 (aromatics).

Cell Culture Experiment

Human aortic endothelial cells (HAECs) were purchased as cryopreserved samples of third passage (Lot: 3F1346) from Cambrex (Wakersville, MD, USA). The HAECs were subcultured once and stored in liquid nitrogen until cell culture experiment. The HAECs used in the experiment were fourth passage. Each well of a 12-well plate of polystyrene (Iwaki) was filled with 1 mL of a supplemented culture medium (EGM-2; Lot: 08103123, Cambrex) and equilibrated at 37 °C in a humidified incubator under 5% CO_2 for 30 min before cell seeding. After the frozen cells were thawed at 37 °C, 10 μL of the cell suspension was seeded in each well. The initial cell density was 2.2×10^3 cells·cm^{-2}. Cell viability assessed by the trypan blue exclusion test was 83% for the cell suspension. The cell seeded plates were placed in a humidified incubator at 37 °C under 5% CO_2. The HAECs were cultured for 48 h. Cell culture mediums were replaced with fresh medium 24 h after cell seeding. At 48 h after cell seeding, cell culture mediums were each replaced with an aqueous suspension of copolymer **8**. Then the HAECs were cultured in the polymer suspension for 1, 6, and 24 h in a humidified incubator at 37 °C under 5% CO_2 to study cellular uptake of nanoaggregates of copolymer **8**. For fluorescence microscopy observation, the cells were fixed by immersion in 10% formaldehyde neutral buffer solution (Nacalai Tesque) at room temperature (22 °C) for 15 min and were washed three times with phosphate-buffered saline (PBS; Gibco). Fluorescence images of the cells were taken with a fluorescence microscope (IX71; Olympus) equipped with a CCD camera (DP70; Olympus). Fluorescence intensity of the incorporated copolymer **8** was measured by integrating the fluorescence intensity observed at each pixel of the fluorescence images using image analysis software (Fluoview ver. 5.0; Olympus).

Measurements

NMR spectra were recorded on a JEOL ECA 600 spectrometer. Optical rotations were measured with a Jasco P-1030 digital polarimeter. GPC analyses were performed by using a TOSOH 8012 with refractive index detection under the following conditions: Shodex Asahipak GF-310HQ column with water as eluent at a flow rate of 0.5 mL·min^{-1}. The calibration curve was obtained using pullulan standards. CD and UV-vis spectra were measured in a quartz cell (thickness 1 cm) at room temperature using a Jasco J-820 spectropolarimeter and Shimadzu UV160A spectrophotometer, respectively. The SEM images were obtained using a Hitachi S-4100 electron microscope. The DLS measurement was performed on a Zetasizer 3000 (Malvern Instruments). Fluorescence spectra were obtained on a fluorescence spectrometer (Shimadzu) using a quartz cuvette (1-mm path length).

Results and Discussion

Copolymerization of 1 with 5

The polymerization of monosubstituted acetylene derivatives has been widely investigated using Rh complex catalysts, which enables stereoselective synthesis of the corresponding polyacetylenes of the *cis*-isomers.[16] As

already reported in our previous publication, **1** was polymerized using (nbd)Rh$^+$ B$^-$(C_6H_5)$_4$ as the catalyst at around 25 °C to 50 °C in a mixed solvent of THF and water (9:1, v/v).[12] In this study, we performed the copolymerization of **1** with **5** under similar conditions. The copolymerization with various feed ratios of **1** to **5** was carried out using the Rh catalyst (5.0 mol-% for **1** + **5**) at 30 °C in a THF-water mixed solvent under argon. After polymerization, the resulting mixture was concentrated and then dissolved in DMSO. The solution was poured into a large amount of methanol to precipitate the polymeric product. The precipitate was isolated by filtration and dried under reduced pressure to give the copolymer **6** (Table 1). The copolymer was soluble in water and DMSO, and its $\overline{M}_n$ value was estimated by GPC analysis with water as eluent using pullulan standards. Figure 1a shows the ^{1}H NMR spectrum of the copolymer (entry 1, Table 1) measured in DMSO-d_6. The signals due to the sugar and alkyl protons are observed at around δ 3.0–4.3 (signals **e–h**) and δ 0.84, 1.21, 1.45, 2.15 (signals **a–d**), respectively. In addition to these signals, signal **i** ascribed to the main-chain proton of –CH=C– appears centered at δ 6.11. The chemical shift of this signal realistically corresponds to the *cis*-isomer. Furthermore, there is no signal due to the *trans*-isomer at lower magnetic field from the *cis*-signal. The NMR results support structure **6** as that of the copolymer, which is mainly composed of *cis*-isomer. The unit ratio of the copolymer is calculated by the integrated ratio of signal **a** and signal **i**.

Table 1 shows the copolymerization results obtained by the various feed ratios of **1** to **5**. The yields and the $\overline{M}_n$ values are 57.0–78.1% and 5 200–9 700, respectively. The unit ratios of **5** in the copolymers increase with increasing molar ratios of **5** in the feeds. In all cases, however, the ratios of **5** in the copolymers are lower than those in the feeds. This is probably because the copolymers with higher

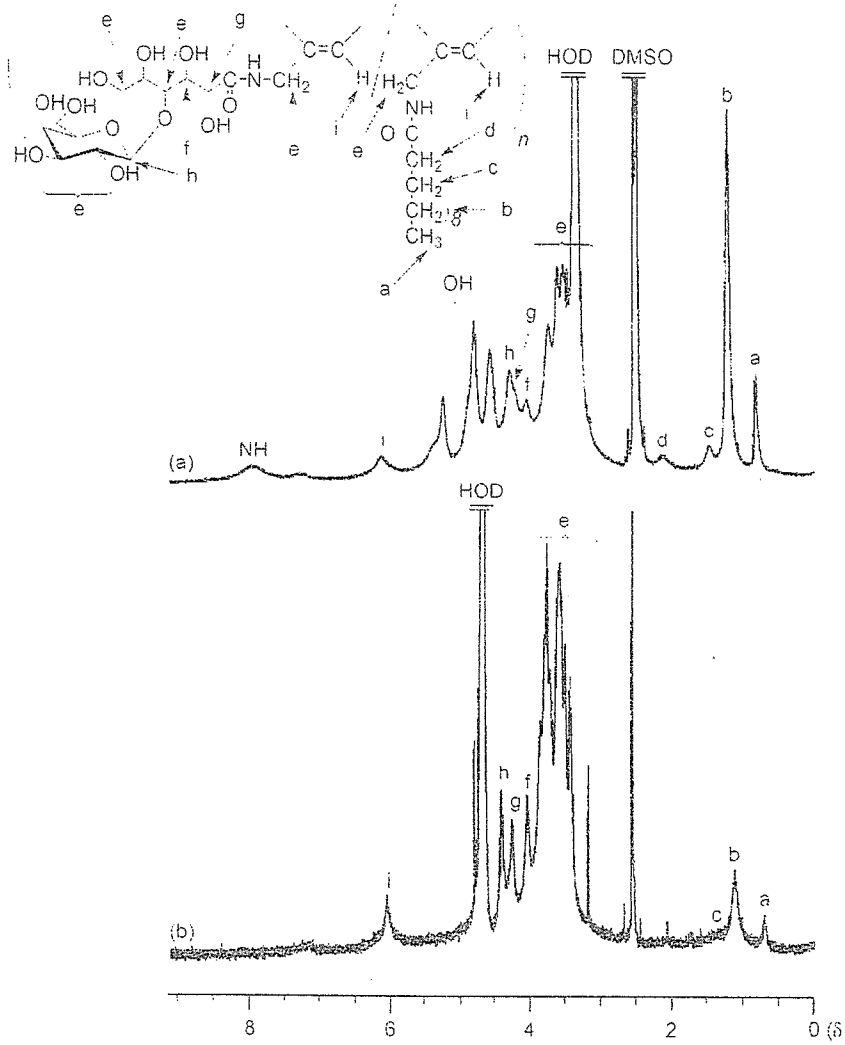

Figure 1. ^{1}H NMR spectra of copolymer **6** (entry 1, Table 1) in DMSO-d_6 (a) and D_2O (b).

contents of the unit **5** are lost as methanol-soluble fractions during the isolation procedure. The optical rotations of the copolymers with the higher contents of the sugar units were larger than those with the lower contents.

Formation of Molecular Aggregates in Water

When the copolymerization was followed by thin-layer chromatography (TLC) on silica gel (methanol: chloroform = 2:1 for **1**; hexane: ethyl acetate = 1:1 for **5**), **1** appeared to be consumed at the early stage of the reaction; subsequently, the consumption of **3** at a later stage was confirmed. This indicated that **6** had the block copolymeric sequence between the unit **1** and the unit **5** rather than in random style. In fact, the intensities of the alkyl signals **a–d** in the ^{1}H NMR spectrum of **6** in D_2O (Figure 1b) are obviously lower than those of the same copolymer measured in DMSO-d_6 (Figure 1a). The NMR results suggest formation of micelle-like aggregates having the outer hydrophilic sugar residues and the inner hydrophobic lauryloyl groups in water, and this was attributed to the block copolymeric sequence. The formation of molecular aggregates of **6** in water was also confirmed by the GPC measurements on aqueous solutions of **6** (entry 5, Table 1, the unit ratio of **1** to **5** = 1.0:0.26) ranging in concentration from 0.05 to 9.0 mg · mL^{-1}. Figure 2 shows the relations of the $\overline{M}_n$ values to the sample concentrations in the GPC experiments. The $\overline{M}_n$ values increase from ca. 6 300 to ca. 11 000 for concentrations higher than 0.70 mg · mL^{-1}. These data suggest the formation of molecular aggregates for the higher concentrations of **6** in water. The molecular aggregates of **6** were directly observed by SEM. The SEM image of the spin-coated sample from the aqueous solution of **6** (entry 4, Table 1, the unit ratio of **1** to **5** = 1.0:0.32) on aluminium plate (Figure 3) shows the particle-type molecular aggregates with average diameters of 20–40 nm. The particle sizes were also confirmed by DLS measurement. The mean particle diameter of the sample shown as entry 4 in Table 1 was 85.2 ± 14.1 nm. The difference in the aggregate sizes obtained by SEM and DLS can be attributed to the difference in the sample condition: dry for SEM and wet for DLS.

Secondary Conformation of 6

We already reported in our previous report that the CD spectrum of the homopolymer **2** in water showed the positive Cotton effect at 330 nm corresponding to the main-chain UV-vis absorption.[12] This indicated the possibility for formation of a one-handed helical conformation in the main chain of **2**. In this study, the CD analysis was also performed to reveal the secondary conformation of copolymer **6**. Figure 4 shows the CD spectra of **6** (entry 5, Table 1, unit ratio of **1** to **5** = 1.0:0.26) in comparison with those of copolymer **4** (unit ratio of **1** to **3** = 1.0: 0.39) measured in DMSO and water at room temperature. The CD spectrum of **6** in DMSO (Figure 4a) shows the positive Cotton effect at 360 nm, corresponding to the main-chain UV-vis absorption. The positive Cotton effect also appeared at this region in the CD spectrum in water (Figure 4b), although its intensity was lower than that in DMSO. It has been reported that the helical structure of poly(*N*-propargylamide)s is stabilized by the intramolecular hydrogen bonds between the pendant amide groups.[17] In polar solvents such as DMSO and water, therefore, the hydrogen bonds are readily broken to effect destabilization of the helical structure. The helical conformation of **6** in polar solvents is probably stabilized by the bulky substituents in the side chains of sugar and lauryloyl groups. These bulky groups shield the hydrogen bonds from the solvents, which consequently stabilizes the helical structure. This reasoning is also supported by comparison of the CD spectra of copolymer **4** (gray lines in

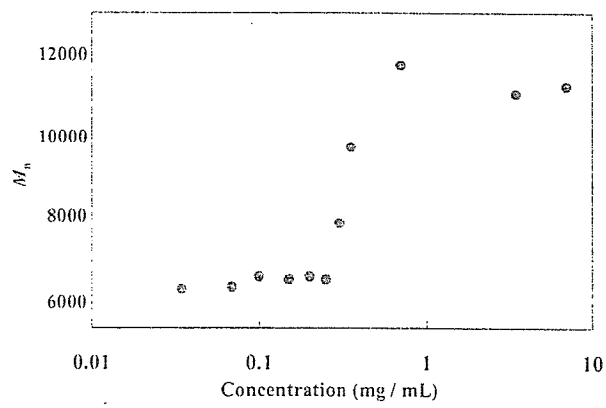

Figure 2. $\overline{M}_n$ values versus sample concentrations in GPC measurements with water as eluent (entry 5, Table 1).

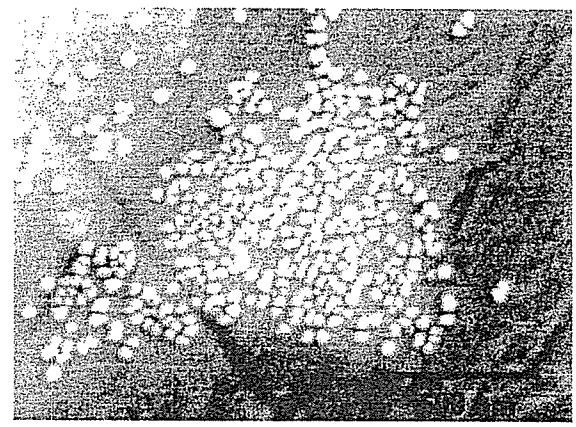

Figure 3. SEM image of **6**: the sample was prepared by spin coating of the dispersed solution of **6** (entry 4, Table 1) in water.

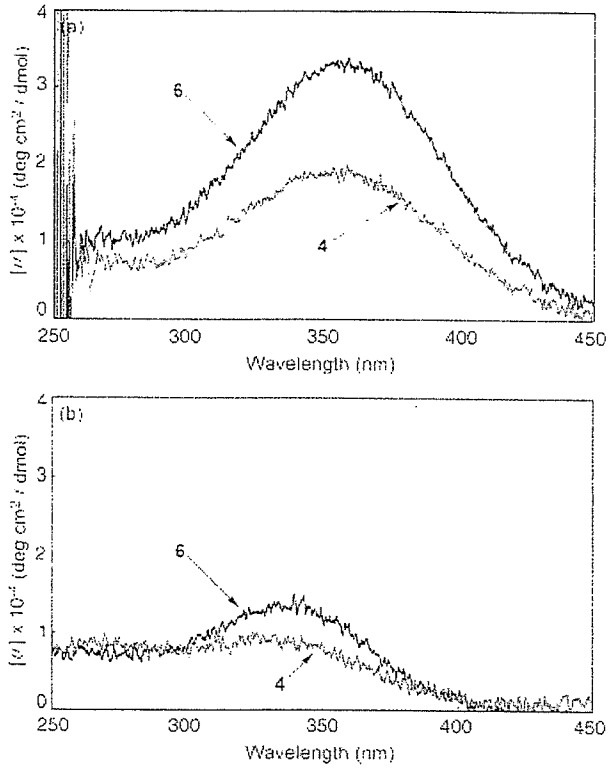

Figure 4. CD spectra of **6** (entry 5, Table 1, unit ratio: **1**:**5** = 1.0:0.26) and **4** (unit ratio: **1**:**3** = 1.0:0.39) in DMSO (a) and water (b) (c = 0.2 mmol·L^{-1}).

Figure 4a, b), which has the less bulky hexanoyl groups. The CD spectra of **4** show weaker Cotton effects than those of **6**, indicating the stabilization of the helical conformation as a result of the bulkiness of the pendant groups.

Cellular Uptake of Amphiphilic Copolymer 8

To evaluate cell uptake of the copolymer by fluorescence microscopy, the rhodamine B dye moiety was introduced into the amphiphilic copolymer. First, an *N*-propargylamide derivative **7** having a pendant rhodamine B moiety was prepared by condensation of *N*-propargylamine hydrochloride with rhodamine B in the presence of a condensing agent (1-[(3-dimethylamino)propyl]-3-ethylcarbodiimide hydrochloride) in methanol. Then, the isolated **7** was copolymerized with **1** and **5** under conditions similar to those described above (Scheme 3). Although **7** did not have homopolymerizability by Rh catalyst, the unit from **7** was slightly incorporated into the resulting terpolymer by the copolymerization. The existence of the rhodamine B moiety in the obtained terpolymer **8** was confirmed by appearance of the signals due to methyl protons of N-CH_2CH_3 as well as the aromatic protons in the ^{1}H NMR spectrum of the product. However, the intensities of the signals were too weak to determine the exact content of the dye moiety in the copolymer by the integration ratio. For comparison, hydrophilic copolymer **9** was synthesized by copolymerization of monomer **1** with monomer **7** using Rh catalyst (Figure 5).

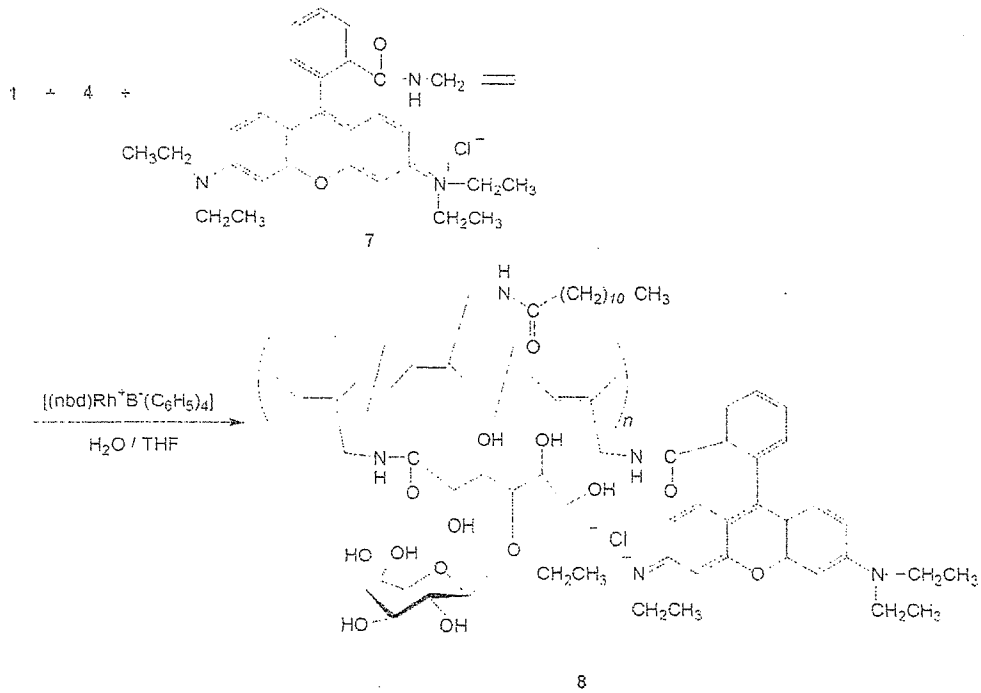

Scheme 3. Terpolymerization of **1**, **5**, and **7**.

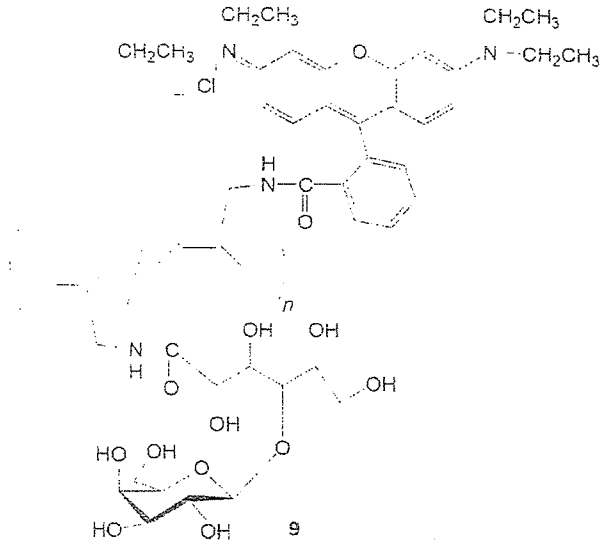

Figure 5. Structure of copolymer 9.

The cell uptake of terpolymer 8 was studied by culturing human aortic endothelial cells (HAECs) in a culture medium containing the terpolymer 8. Ten milligrams of 8 was suspended in 10 mL of culture medium EGM-2 and stirred for 3 h at room temperature. The suspension of 8 was sonicated at 25 W and 40 kHz for 5 min in an ultrasonic bath. The sonication was repeated twice. The obtained suspension was filtered through membrane filters with the pore sizes of 0.45 μm and 0.2 μm for sterilization. An aqueous solution of polymer 9 was prepared by following the above procedure. To evaluate the concentration of 8, a calibration curve (data not shown) was obtained by using the aqueous solution of 9 (1 mg · mL^{-1}) as a standard polymer sample to relate concentration to fluorescence intensity. The concentration of 8 was estimated to be 0.09 mg · mL^{-1} by using the calibration curve. The DLS measurement revealed that the polymer aggregates (nanoparticles) of 8 have a mean diameter of 114.9 ± 32 nm in a culture medium containing 10% bovine serum. HAECs were exposed to the polymer aggregates of 8 while they were cultured in the culture medium containing the amphiphilic polymer 8. After the prescribed period of culture, 1, 6, or 24 h, the HAECs were fixed in 10% formaldehyde neutral buffer solution for microscope observation. Figure 6 shows phase contrast (a), fluorescence (b), and merged (phase contrast + fluorescence) (c) images of HAECs after 24 h of incubation. The merged image demonstrates that red fluorescent light of rhodamine B was emitted from the sites where HAECs were located. This indicates that the polymer aggregates of 8 were incorporated into HAECs. The fluorescence images at each time of incubation are shown in Figure 7. The fluorescence images get brighter with the incubation time. To quantitatively evaluate cell uptake of nanoaggregates, fluorescence intensity per image (1 360 × 1 024 pixels) was determined by integrating the brightness at each pixel of the fluorescence image using image analysis software. The

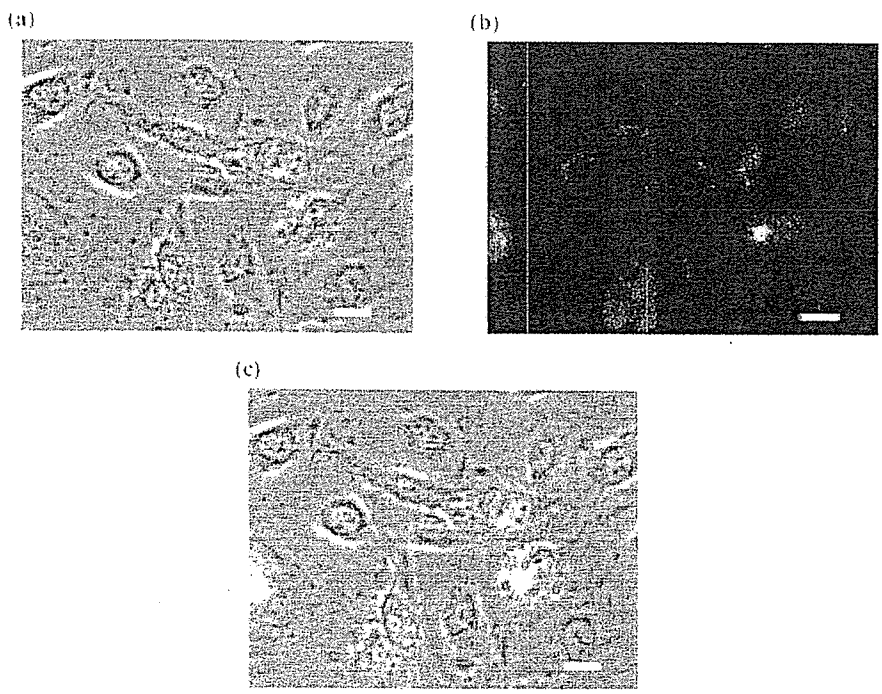

Figure 6a–c. Localization of rhodamine B-labeled copolymer 8 in human aortic endothelial cells. Phase contrast image (a), fluorescence image (b), and merged image of (a) and (b). Bars: 20 μm.

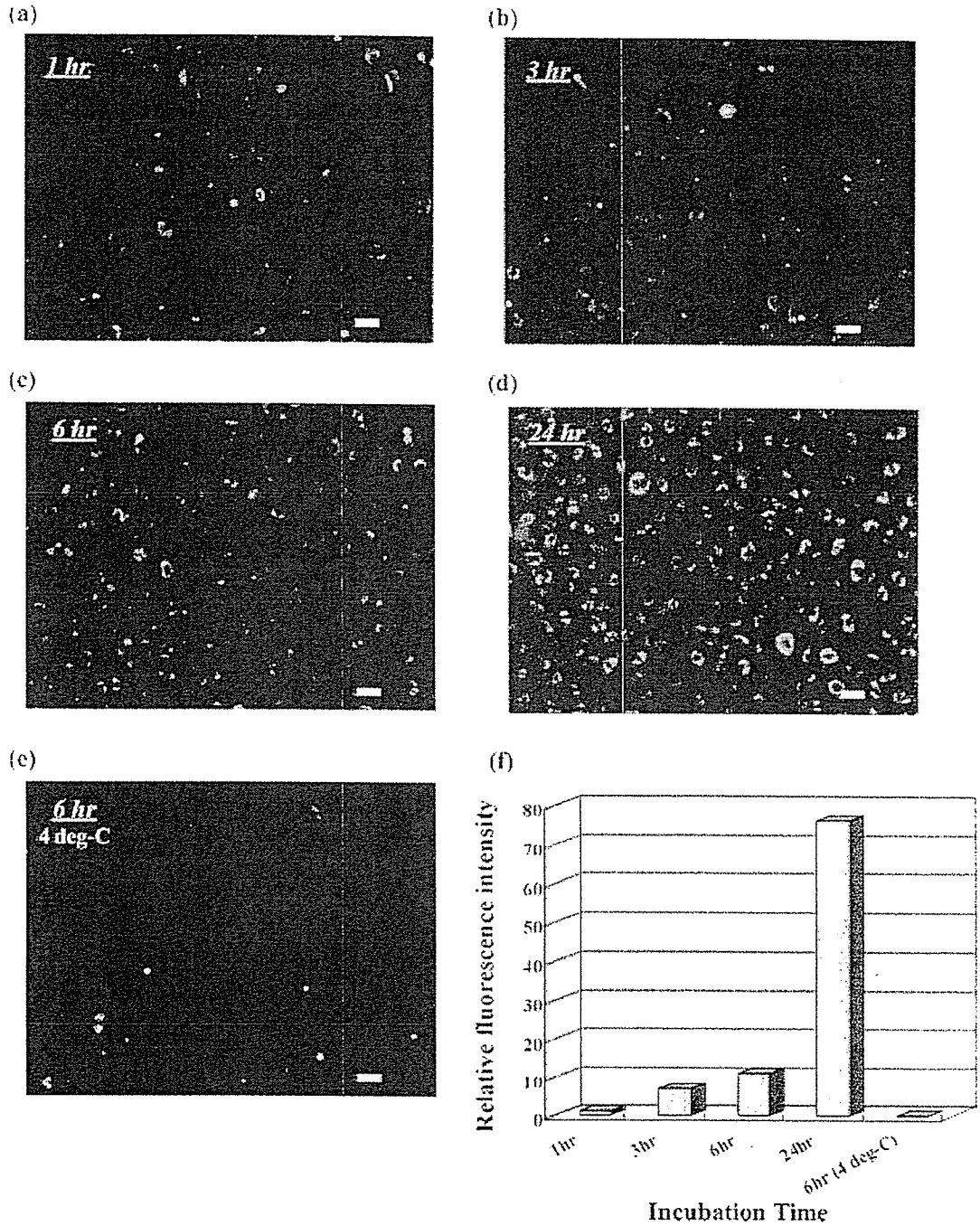

Figure 7a–f. Uptake of rhodamine B-labeled copolymer **8** by human aortic endothelial cells: incubation time, 1 h (a), 3 h (b), 6 h (c), 24 h (d) (incubation at 37 °C), and 6 h (incubation at 4 °C) (e). Bars: 20 μm. The uptake is quantitatively represented as relative fluorescence intensity in the bar graph (f).

fluorescence intensity was normalized in a ratio of the fluorescence intensity at each incubation time to that at 1 h of incubation. The ratio was termed as the relative fluorescence intensity. The time course of the relative fluorescence intensity is shown in Figure 7f and indicates that HAECs incorporated progressively more nanoaggregates of **8** during the incubation time. The relative fluorescence intensity was 7-fold at 3 h, 11-fold at 6 h, and 76-fold at 24 h of incubation. In contrast, the relative fluorescence intensity dropped considerably and was only 12% of the control level (1 h at 37 °C) when HAECs were exposed to the nanoaggregates of **8** at 4 °C for 6 h. The fact that the temperature triggered a dramatic decrease in the relative fluorescence intensity suggests that the nanoag-

gregates are incorporated into HAECs by endocytosis. Endocytosis is known as a cellular process that is coupled with temperature-dependent metabolic activities.[18] Furthermore, it is known that some receptors and membrane microdomains of endothelial cell are involved in endocytosis.[19] However, it is not clear which of the endocytic pathways is responsible for the uptake of the nanoaggregates. This issue is now under investigation.

Conclusion

In this study, we investigated synthesis of the amphiphilic poly(*N*-propargylamide) **6** containing both sugar residues (hydrophilic part) and long alkyl chains (hydrophobic part) in order to develop a novel nanoaggregate based on the self-organization of amphiphilic polymers with rigid backbone. The desired polymer was prepared by copolymerization of the two *N*-propargylamide monomers **1** and **5** having a galactose residue and a lauryloyl group, respectively, catalyzed by a Rh complex. The GPC, ^{1}H NMR, SEM, and DLS analyses of the resulting copolymers indicated formation of the nanoparticles in water. The formation of the one-handed helical conformation of the copolymer in both DMSO and water was confirmed by the CD spectra. An amphiphilic poly(*N*-propargylamide) containing fluorescent dyes was newly designed to evaluate cell uptake of nanoparticles of the amphiphilic copolymer by fluorescence microscopy. The *N*-propargylamide monomer **7**, having a rhodamine B dye moiety, was prepared and copolymerized with **1** and **5**. Human aortic endothelial cells (HAECs) were cultured in a medium containing the fluorescent-dye-labeled amphiphilic copolymer. Cell uptake of the copolymer was confirmed by red fluorescence emission from each of the HAECs. Progressive uptake was observed during the incubation period. When the cell culture experiment was conducted at 4 °C, the fluorescence intensity of the red emission was considerably lowered. This indicates that the cell uptake is inhibited at 4 °C and that this uptake process should occur in an endocytic pathway rather than by simple adsorption to the plasma membrane of HAECs. We are now synthesizing a fluorescent-dye-labeled hydrophilic copolymer of monomer **1** with monomer **7** to study preferential cell uptake of the nanoaggregates of the amphiphilic copolymer. In the future, we anticipate that nanoparticles will be able to be preferentially endocytosed into cells rather than monomeric chains of water-soluble copolymer. If this does occur, the nanoparticles of the amphiphilic copolymer will be a promising nanocarrier for drug delivery.

Acknowledgements: This work was financially supported by the *Asahi Glass Foundation*. The author (T. N.) thanks Professor *Mitsuru Akashi* of Osaka University and Dr. *Takami Akagi* of the Japan Science and Technology Agency for dynamic light scattering measurement. The author (T. N.) thanks Dr. *Tetsuji Yamaoka* and Dr. *Atsushi Mahara* of the National Cardiovascular Center Research Institute for fluorescence spectroscopy analysis.

[1] M. Okada, *Prog. Polym. Sci.* **2001**, *26*, 67.
[2] Y. C. Lee, R. T. Lee, "*Neoglycoconjugates: Preparation and Applications*", Academic Press, San Diego **1994**.
[3] K. Kobayashi, A. Tsuchida, T. Usui, T. Akaike, *Macromolecules* **1997**, *30*, 2016.
[4] K. Kobayashi, N. Kakishita, M. Okada, T. Akaike, T. Usui, *J. Carbohydr. Chem.* **1994**, *13*, 753.
[5] L. L. Kiessling, N. L. Pohl, *Chem. Biol.* **1996**, *3*, 71.
[6] M.-G. Baek, R. C. Stevens, D. H. Charych, *Bioconjugate Chem.* **2000**, *11*, 777.
[7] L.-B. Kim, B. Erdogan, J. N. Wilson, U. H. F. Bunz, *Chem. Eur. J.* **2004**, *10*, 6247.
[8] T. Hasegawa, S. Kondoh, K. Matsuura, K. Kobayashi, *Macromolecules* **1999**, *32*, 6595.
[9] J. Kadokawa, Y. Shinmen, S. Shoda, *Macromol. Rapid Commun.* **2005**, *26*, 103.
[10] A. Takasu, K. Iso, T. Dohmae, T. Hirabayashi, *Biomacromolecules* **2006**, *7*, 411.
[11] K. Matsuura, S. Furuno, K. Kobayashi, *Chem. Lett.* **1998**, 847.
[12] J. Kadokawa, K. Tawa, M. Suenaga, Y. Kaneko, M. Tabata, *J. Macromol. Sci., Pure Appl. Chem.* **2006**, *43*, 1179.
[13] J. Deng, J. Tabei, M. Shiotsuki, F. Sanda, T. Masuda, *Macromolecules* **2004**, *37*, 9715 and references therein.
[14] R. R. Shrock, J. A. Osborn, *Inorg. Chem.* **1970**, *9*, 2339.
[15] J. Deng, J. Tabei, M. Shiotsuki, F. Sanda, T. Masuda, *Macromolecules* **2004**, *37*, 1891.
[16] M. Tabata, T. Sone, Y. Sadahiro, *Macromol. Chem. Phys.* **1999**, *200*, 265.
[17] J. Tabei, R. Nomura, T. Masuda, *Macromolecules* **2002**, *35*, 5405.
[18] G. Durin, S. Cottin, E. Blanc, A. R. Rees, *J. Temsamani, J. Biol. Chem.* **2003**, *278*, 31192.
[19] S. Muro, M. Koval, V. Muzykantov, *Curr. Vasc. Pharmacol.* **2004**, *2*, 281.

Am J Physiol Heart Circ Physiol 291: H1138–H1146, 2006.
First published April 28, 2006; doi:10.1152/ajpheart.00187.2006.

Cardioprotective role of endogenous hydrogen peroxide during ischemia-reperfusion injury in canine coronary microcirculation in vivo

Toyotaka Yada,[1] Hiroaki Shimokawa,[3] Osamu Hiramatsu,[1] Yoshisuke Haruna,[2] Yoshitaka Morita,[2] Naoki Kashihara,[2] Yoshiro Shinozaki,[4] Hidezo Mori,[5] Masami Goto,[1] Yasuo Ogasawara,[1] and Fumihiko Kajiya[1]

[1]*Department of Medical Engineering and Systems Cardiology and* [2]*Division of Nephrology and Rheumatology, Department of Internal Medicine, Kawasaki Medical School, Kurashiki;* [3]*Department of Cardiovascular Medicine, Tohoku University Graduate School of Medicine, Sendai;* [4]*Department of Physiology, Tokai University School of Medicine, Isehara; and* [5]*Department of Cardiac Physiology, National Cardiovascular Center Research Institute, Suita, Japan*

Submitted 22 February 2006; accepted in final form 18 April 2006

Yada, Toyotaka, Hiroaki Shimokawa, Osamu Hiramatsu, Yoshisuke Haruna, Yoshitaka Morita, Naoki Kashihara, Yoshiro Shinozaki, Hidezo Mori, Masami Goto, Yasuo Ogasawara, and Fumihiko Kajiya. Cardioprotective role of endogenous hydrogen peroxide during ischemia-reperfusion injury in canine coronary microcirculation in vivo. *Am J Physiol Heart Circ Physiol* 291: H1138–H1146, 2006. First published April 28, 2006; doi:10.1152/ajpheart.00187.2006.—We have recently demonstrated that endogenous H_2O_2 plays an important role in coronary autoregulation in vivo. However, the role of H_2O_2 during coronary ischemia-reperfusion (I/R) injury remains to be examined. In this study, we examined whether endogenous H_2O_2 also plays a protective role in coronary I/R injury in dogs in vivo. Canine subepicardial small coronary arteries (≥100 μm) and arterioles (<100 μm) were continuously observed by an intravital microscope during coronary I/R (90/60 min) under cyclooxygenase blockade ($n = 50$). Coronary vascular responses to endothelium-dependent vasodilators (ACh) were examined before and after I/R under the following seven conditions: control, nitric oxide (NO) synthase (NOS) inhibitor N^G-monomethyl-L-arginine (L-NMMA), catalase (a decomposer of H_2O_2), 8-sulfophenyltheophylline (8-SPT, an adenosine receptor blocker), L-NMMA + catalase, L-NMMA + tetraethylammonium (TEA, an inhibitor of large-conductance Ca^{2+}-sensitive potassium channels), and L-NMMA + catalase + 8-SPT. Coronary I/R significantly impaired the coronary vasodilatation to ACh in both sized arteries (both $P < 0.01$); L-NMMA reduced the small arterial vasodilatation (both $P < 0.01$), whereas it increased ($P < 0.05$) the ACh-induced coronary arteriolar vasodilatation associated with fluorescent H_2O_2 production after I/R. Catalase increased the small arterial vasodilatation ($P < 0.01$) associated with fluorescent NO production and increased endothelial NOS expression, whereas it decreased the arteriolar response after I/R ($P < 0.01$). L-NMMA + catalase, L-NMMA + TEA, or L-NMMA + catalase + 8-SPT further decreased the coronary vasodilatation in both sized arteries (both, $P < 0.01$). L-NMMA + catalase, L-NMMA + TEA, and L-NMMA + catalase + 8-SPT significantly increased myocardial infarct area compared with the other four groups (control, L-NMMA, catalase, and 8-SPT; all, $P < 0.01$). These results indicate that endogenous H_2O_2, in cooperation with NO, plays an important cardioprotective role in coronary I/R injury in vivo.

endothelium-derived relaxing factor; myocardial infarction; vascular endothelial function

VASCULAR ENDOTHELIAL CELLS play an important role in maintaining vascular homeostasis by synthesizing and releasing endothelium-derived relaxing factors (EDRFs), including prostacyclin (PGI_2), nitric oxide (NO), and endothelium-derived hyperpolarizing factor (EDHF) (6, 9, 26). Endothelial dysfunction is thus characterized by a reduction in the activity of PGI_2, NO, and EDHF, thereby enhancing vasoconstrictor responses mediated by endothelin, serotonin, and thrombin (26). Endothelial injury secondary to myocardial ischemia-reperfusion (I/R) decreases the production and activity of EDRFs in acute myocardial infarction (18).

Among the three different EDRFs, the roles of PGI_2 and NO have been extensively investigated (6, 9, 26). Regarding EDHF, since the first reports on its existence (6, 9), several candidates for EDHF have been proposed, including cytochrome *P*-450 metabolites (2, 4), endothelium-derived K^+ (7), and electrical communications through gap junctions between endothelial cells and vascular smooth muscle cells (29). Matoba et al. (16, 17) have previously identified that endothelium-derived H_2O_2 is a primary EDHF in mesenteric arteries of mice and humans. Morikawa et al. (21) have recently confirmed that endothelial Cu,Zn-SOD plays an important role as an EDHF synthase in mice. We have subsequently confirmed the importance of H_2O_2 in canine coronary microcirculation during coronary autoregulation with reduced coronary perfusion pressure in vivo (35).

However, it remains to be examined whether H_2O_2 also exerts cardioprotective effects during I/R in the coronary microcirculation in vivo, and if so, whether such effects of H_2O_2 compensate the impaired NO-mediated responses due to I/R injury in vivo. In this study, we tested our hypothesis that H_2O_2 plays an important cardioprotective and compensatory role during coronary I/R injury in dogs in vivo.

METHODS

This study conformed to the Guideline on Animal Experiments of Kawasaki Medical School, and approved by an independent review committee from the same institution, and the *Guide for the Care and Use of Laboratory Animals* published by the National Institutes of Health.

Animal preparation. Anesthetized mongrel dogs (15–25 kg in body wt, $n = 50$) of either sex were ventilated with a ventilator (model VS600, IDC, Pittsburgh, PA). Aortic pressure and left ventricular (LV) pressure were continuously monitored with a catheter (SPC-784A, Millar, TX). The blood flow of the left anterior descending coronary artery (LAD) was continuously measured by a transonic flow probe (T206, Transonic Systems, Ithaca, NY).

Address for reprint requests and other correspondence: T. Yada, Dept. of Medical Engineering and Systems Cardiology, Kawasaki Medical School, 577 Matsushima, Kurashiki, Okayama 701-0192, Japan (e-mail: yada@me.kawasaki-m.ac.jp).

The costs of publication of this article were defrayed in part by the payment of page charges. The article must therefore be hereby marked "*advertisement*" in accordance with 18 U.S.C. Section 1734 solely to indicate this fact.

Measurements of coronary diameter by intravital microscope. We continuously monitored coronary vascular responses by an intravital microscope (VMS 1210, Nihon-Kohden, Tokyo) with a needle probe in vivo as previously described (32). We gently placed the needle probe on subepicardial microvessels. When a clear vascular image was obtained, end-diastolic vascular images were taken with 30 pictures/s (32).

Measurements of regional myocardial blood flow. Regional myocardial blood flow was measured by the nonradioactive microsphere (Sekisui Plastic, Tokyo) technique, as previously described (20). Briefly, the microsphere suspension was injected into the left atrium 85 min after the onset of coronary occlusion. Myocardial collateral flow in the apex during suturing of the collateral vessels from the left circumflex artery (LCX) was calculated according to the formula: time flow = tissue counts × (reference flow/reference counts) and was expressed in milliliters per gram per minute (20).

Detection of H_2O_2 and NO production. 2′,7′-Dichlorodihydrofluorescein diacetate (DCF, Molecular Probes, Eugene, OR) and diaminorhodamine-4M AM (DAR, Daiichi Pure Chemicals, Tokyo) were used to detect H_2O_2 and NO production in coronary microvessels without a different NO scavenger (e.g., methylene blue), respectively, as previously described (21). Briefly, fresh and unfixed heart tissue was cut into several blocks and frozen in optimal cutting temperature compound (Tissue-Tek, Sakura Fine Chemical, Tokyo) within a few hours. Fluorescent images of [illegible] after application of ACh by using [illegible] pus BX51, Tokyo) (21). We used different animals for the fluorescent treatment (DCF and DAR) and the 2,3,5-triphenyltetrazolium chloride (TTC) treatment.

Western blotting. Portions of myocardial samples were homogenized in lysis buffer. After centrifugation, the supernatants were used for Western immunoblotting. The proteins were transferred by semidry electroblotting to polyvinylidene difluoride membranes. The blots were then blocked and incubated with horseradish peroxidase-conjugated rabbit anti-endothelial NO synthase (eNOS, dimer form) polyclonal antibody (Santa Cruz Biotechnology, Santa Cruz, CA) or anti-actin antibody (Santa Cruz Biotechnology). The antibody was visualized by using an enhanced chemiluminescence method (ECL; Amersham Biosciences, Tokyo). The integrated density of the bands was quantified by using NIH Image analysis, and the protein expression level of eNOS was normalized to that of actin (24).

Experimental protocols. After the surgical procedure and instrumentation, at least 30 min was allowed for stabilization while hemodynamic variables were monitored. The following protocols were examined.

Coronary vascular responses to endothelium-dependent [ACh, 0.5 and 1.0 μg/kg intracoronary (ic)] and -independent [sodium nitroprusside (SNP), 40 and 80 μg/min ic] vasodilators were examined before ischemia (90 min)-reperfusion (60 min) (I/R). ACh and SNP were continuously and retrogradely infused into the diagonal branch of the LAD by using a syringe pump (STC 525, Terumo, Tokyo). The coronary vascular responses to ACh and SNP were examined for 2 min, and the image of maximal vasodilatation was taken at 2 min of infusion of ACh or SNP.

Coronary vasodilator responses to ACh and SNP were examined before and after coronary ischemia (90 min)-reperfusion (60 min) by proximal LAD occlusion under the following seven conditions with cyclooxygenase blockade (ibuprofen, 12.5 mg/kg iv) to evaluate the [illegible] and NO [illegible] about PGI_2 in a different set of animals (Fig. [illegible] N^G-monomethyl-L-arginine (L-NMMA) [illegible] and 240,000 U·kg^{-1}·min^{-1} ic for 10 min, an inhibitor of endogenous H_2O_2 into water and oxygen), *4*) adenosine receptor blockade alone [8-sulfophenyltheophylline (8-SPT), 25 μg·kg^{-1}·min^{-1} ic for 5 min], *5*) catalase plus L-NMMA, *6*) catalase plus tetraethylammonium [TEA, 10 μg·kg^{-1}·min^{-1} ic for 10 min, an inhibitor of large-

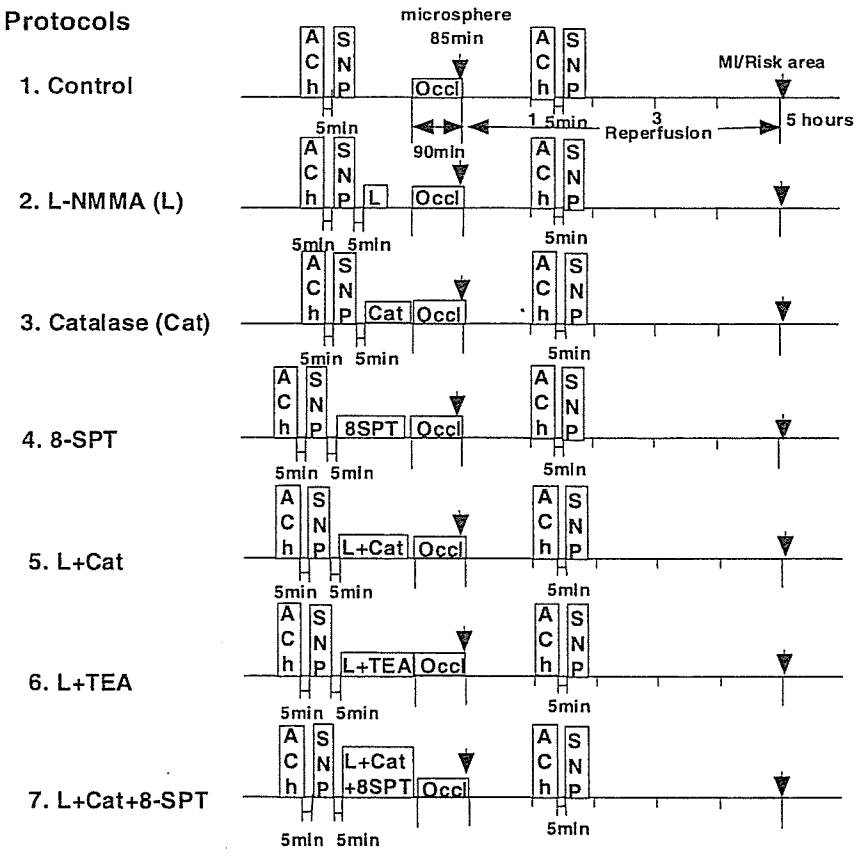

Fig. 1. Experimental protocols. TEA, tetraethylammonium; 8-SPT, 8-sulfophenyltheophylline; ACh, acetylcholine; SNP, sodium nitroprusside; Occl, coronary occlusion; Cat, catalase; L-NMMA (L), N^G-monomethyl-L-arginine; MI, myocardial infarction.

Table 1. *Hemodynamics during coronary ischemia-reperfusion injury in dogs*

		Before I/R			Ischemia (85 min)	After I/R		
	n	Baseline	ACh	SNP		Baseline	ACh	SNP
MBP, mmHg								
Control	5	92±4	91±6	92±5	93±14	92±4	91±5	92±6
L-NMMA	5	97±8	98±7	94±9	92±10	97±7	98±8	95±8
Cat	5	96±8	92±8	94±9	92±9	96±7	96±8	98±6
L-NMMA + Cat	5	94±4	93±9	97±9	95±11	95±8	98±5	94±5
L-NMMA + TEA	5	95±12	93±13	95±14	94±10	91±14	93±15	98±10
L-NMMA + Cat + 8-SPT	5	95±3	96±4	95±3	93±11	96±3	97±4	95±3
Heart rate, beats/min								
Control	5	152±5	155±3	154±3	156±7	156±5	154±5	153±5
L-NMMA	5	157±5	156±5	157±6	158±6	153±5	153±5	153±5
Cat	5	155±4	159±6	158±5	157±6	151±7	155±8	154±8
L-NMMA + Cat	5	156±12	158±13	158±13	154±5	156±13	156±14	159±13
L-NMMA + TEA	5	153±13	154±12	155±11	155±5	150±10	151±11	152±10
L-NMMA + Cat + 8-SPT	5	152±7	155±9	153±3	153±5	152±7	151±6	153±7

Results are expressed as means ± SE; *n* = no. of dogs. I/R, ischemia-reperfusion; MBP, mean blood pressure; Cat, catalase; SNP, sodium nitroprusside; TEA, tetraethylammonium; 8-SPT, sulfophenyltheophylline; L-NMMA, N^G-monomethyl-L-arginine.

conductance Ca^{2+}-sensitive potassium (K_{Ca}) channels], and *7*) catalase plus L-NMMA with 8-SPT (35). These inhibitors were given at 30 min before I/R. An interval between each treatment was 5 min. The basal coronary diameter was defined as that before administration of ACh or SNP either before or after I/R. L-NMMA, catalase, TEA, and 8-SPT were administered alone at 5 min after administration of ACh or SNP. Microspheres were administered at 85 min after the initiation of coronary occlusion. In the combined infusion (L-NMMA + catalase + 8-SPT), catalase solution was infused into the LAD at a rate of 0.5 ml/min at 5 min after infusion of L-NMMA, and then 8-SPT was added into the LAD at 15 min after the initiation of L-NMMA.

After 1 h of reperfusion, coronary vasodilator responses to ACh and SNP were examined.

After 5 h of reperfusion, we reoccluded the LAD and injected Evans blue dye into a systemic vein. Then, myocardial slices (5 μm thick) were incubated in 1% TTC (Sigma) solution to detect the infarct area (36). Different animals were used for fluorescent treatment (DCF and DAR) and TTC treatment.

Drugs. All drugs were obtained from Sigma Chemical and were diluted in a physiological saline immediately before use.

Statistical analysis. Results are expressed as means ± SE. Vascular responses (see Figs. 3*C*, 5*F*, 6*F*, 7, and 9*A*) were analyzed by one-way ANOVA followed by Scheffé's post hoc test for multiple comparisons. Difference in the effects of ACh and SNP on subepicardial coronary microvessels before and after I/R (see Figs. 3, *A* and *B*, 4, and 8, *A* and *B*), and difference between infarct size/risk area and transmural collateral flow in control and other inhibitors (see Fig. 9*B*) were examined by a multiple regression analysis by using a model in which the change in coronary diameter was set as a dependent variable (y) and vascular size as an explanatory variable (x), while the statuses of control and other inhibitors were set as dummy variables (D_1, D_2) in the following equation: $y = a_0 + a_1x + a_2D_1 + a_3D_2$, where a_0 through a_3 are partial regression coefficients (36). The criterion for statistical significance was at $P < 0.05$.

RESULTS

Hemodynamics and blood gases during I/R injury. Immediately after reperfusion, coronary blood flow was increased and some arrhythmias occurred; however, those changes returned to the control levels 1 h after reperfusion when we repeated the measurements. Thus, throughout the experiments, mean aortic pressure and heart rate at baseline were constant and comparable, and Po_2, Pco_2, and pH were maintained within the physiological ranges (pH 7.35–7.45, Po_2 > 70 mmHg, and Pco_2 25–40 mmHg,). Hemodynamic variables at baseline did not significantly change after I/R compared with those before I/R (Tables 1 and 2).

Dose responses to ACh and SNP. ACh (0.5 and 1.0 μg/kg ic) and SNP (40 and 80 μg/min ic) caused coronary vasodilatation in a dose-dependent manner at both small arteries and arterioles (Fig. 2). Then we chose the maximal dose of the vasodilators (ACh, 1.0 μg/kg ic, and SNP, 80 μg/min ic) in the following experiments.

Endothelium-dependent coronary vasodilatation before and after I/R. There was no significant difference in baseline diameter after ACh before I/R among the groups. All inhibitors did not affect resting coronary artery diameter or coronary

Table 2. *Baseline vascular diameter before I/R in response to ACh*

	Small Artery	Arteriole
Control	104–150 μm (120±7, *n* = 7)	37–96 μm (70±6, *n* = 12)
L-NMMA	106–164 μm (131±7, *n* = 8)	36–95 μm (63±5, *n* = 16)
Cat	100–147 μm (121±5, *n* = 10)	28–89 μm (61±6, *n* = 12)
8-SPT	114–162 μm (130±8, *n* = 6)	30–88 μm (60±10, *n* = 5)
L-NMMA + Cat	102–141 μm (118±5, *n* = 8)	34–95 μm (77±4, *n* = 10)
L-NMMA + TEA	105–142 μm (123±6, *n* = 5)	34–95 μm (62±9, *n* = 8)
L-NMMA + Cat + 8-SPT	110–145 μm (128±6, *n* = 5)	38–87 μm (67±7, *n* = 7)

Results are expressed as range (means ± SE); *n* = no. of blood vessels.

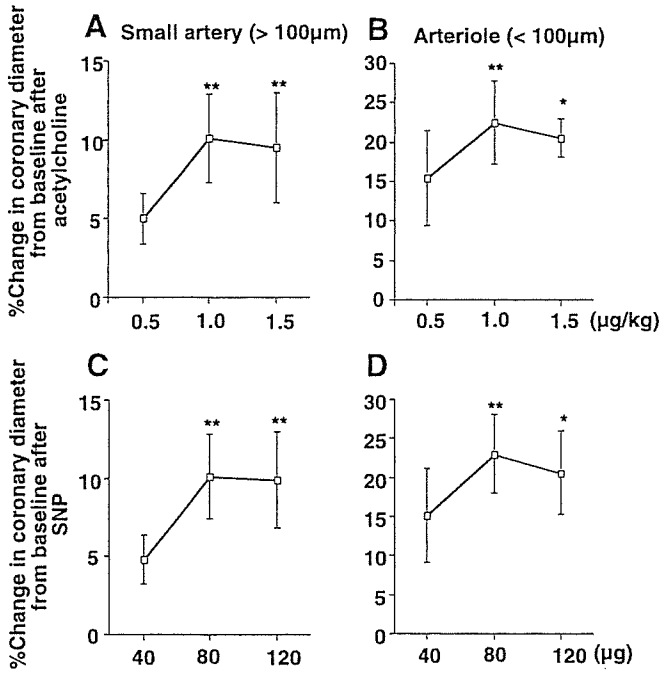

Fig. 2. Dose responses to ACh (*A* and *B*) and SNP (*C* and *D*) before ischemia-reperfusion (I/R). Number of small arteries (*A* and *C*) and arterioles (*B* and *D*) per animals used was 5/5 for each group. $*P < 0.05$, $**P < 0.01$ vs. ACh (0.5 μg/kg) and SNP (40 μg).

blood flow. Under control conditions (before I/R), intracoronary administration of ACh caused a significantly greater coronary vasodilatation in arterioles than in small arteries (Fig. 3, *A* and *B*). Coronary I/R significantly impaired the coronary vasodilatation to ACh in both sized arteries (Figs. 3*A* and 4*A*), and L-NMMA reduced the vasodilatation in small arteries (Figs. 3*A* and 4*B*) but rather increased the response in arterioles compared with control (Figs. 3*B* and 4*A*) after I/R. Catalase and 8-SPT increased the ACh-induced vasodilatation in small arteries (Figs. 3*A* and 4, *C* and *D*) but decreased the response in arterioles (Fig. 3*B*) after I/R. There was no significant difference in coronary blood flow before and after I/R among the control, the L-NMMA, and the catalase group (Fig. 3*C*). L-NMMA + catalase (Figs. 3, *A* and *B*, and 4*E*) or L-NMMA + TEA (Figs. 3, *A* and *B*, and 4*F*) decreased the vasodilatation in both sized arteries (Fig. 3, *A* and *B*) with decrement of coronary blood flow (Fig. 3*C*), and L-NMMA plus catalase with 8-SPT further decreased the vasodilatation in both sized arteries (Figs. 3, *A* and *B*, and 4*G*) compared with other groups (Fig. 3, *A–C*).

Detection of H_2O_2 and NO production. Fluorescent microscopy with DCF showed that I/R increased the vascular H_2O_2 production in control LCX (Fig. 5, *B* and *F*) compared with baseline conditions (Fig. 5, *A* and *F*) and decreased the H_2O_2 production in control LAD (Figs. 5, *C* and *F*), which was enhanced by L-NMMA (Fig. 5, *D* and *F*) and was abolished by catalase (Fig. 5, *E* and *F*) in arterioles. By contrast, the production of NO as assessed with DAR fluorescence was increased in control LCX (Fig. 6, *B* and *F*) compared with baseline LCX (Fig. 6, *A* and *F*) after I/R, decreased in control LAD (Fig. 6, *C* and *F*), inhibited by L-NMMA (Fig. 6, *D* and *F*), and was enhanced by catalase (Fig. 6, *E* and *F*) in small arteries.

Western blotting of eNOS protein expression in myocardium. In the control group, expression of eNOS protein in the ischemic LAD area was significantly decreased compared with the nonischemic LCX area (Fig. 7). In the catalase group, this decrease in the eNOS protein expression was inhibited by catalase (Fig. 7).

Endothelium-independent coronary vasodilatation. Coronary vasodilator responses to SNP were comparable under all conditions in both sized arteries (Fig. 8). Those coronary vasodilator responses were resistant to the blockade of NO synthesis with L-NMMA (Fig. 8).

Effect of H_2O_2 on I/R-induced myocardial infarct size. I/R injury caused myocardial infarction, the size of which was ~40% of the LV risk area (Fig. 9*A*). Intracoronary L-NMMA, catalase, or 8-SPT alone did not further increase the I/R-induced infarct size (Fig. 9*A*). By contrast, intracoronary L-NMMA plus catalase or TEA markedly increased the infarct size, and L-NMMA plus catalase with 8-SPT further increased

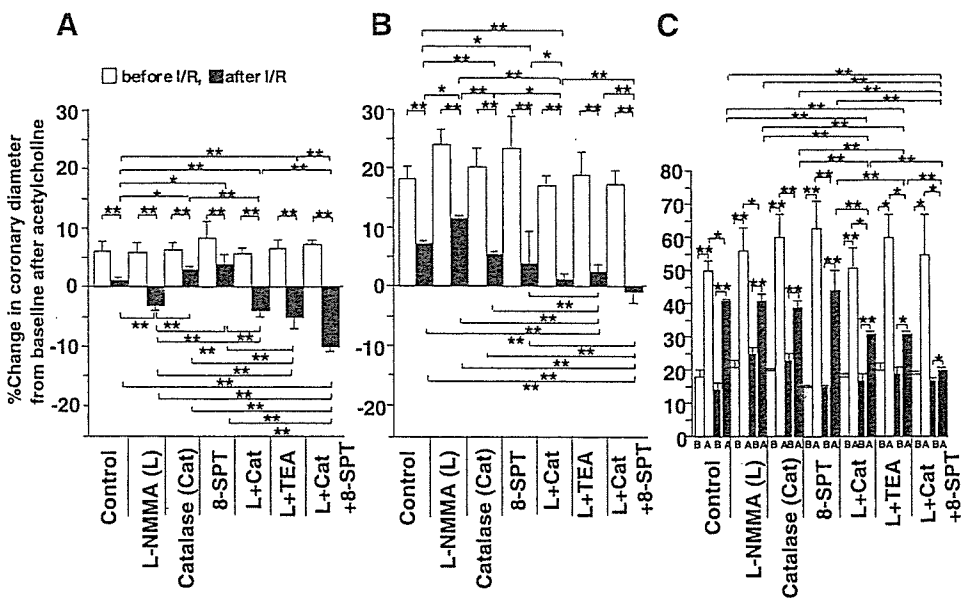

Fig. 3. Endothelium-dependent coronary vasodilatation to ACh before and after coronary I/R injury in dogs in vivo. *A*: small artery (≥100 μm). *B*: arteriole (<100 μm). *C*: coronary blood flow (CBF). No. of small arteries or arterioles per animals (*n*/*n*) used was 7/5 for control, 8/5 for L-NMMA, 10/5 for catalase, 6/5 for 8-SPT, 8/5 for L-NMMA plus catalase, 5/5 for L-NMMA plus TEA, and 5/5 for L-NMMA plus catalase plus 8-SPT in small arteries; and 12/5 for control, 16/5 for L-NMMA, 12/5 for catalase, 5/5 for 8-SPT, 10/5 for L-NMMA plus catalase, 8/5 for L-NMMA plus TEA, and 7/5 for L-NMMA plus catalase plus 8-SPT in arterioles. No. of animals during the measuring CBF used was 5 for each group. B, before ACh; A, after ACh. $*P < 0.05$, $**P < 0.01$.

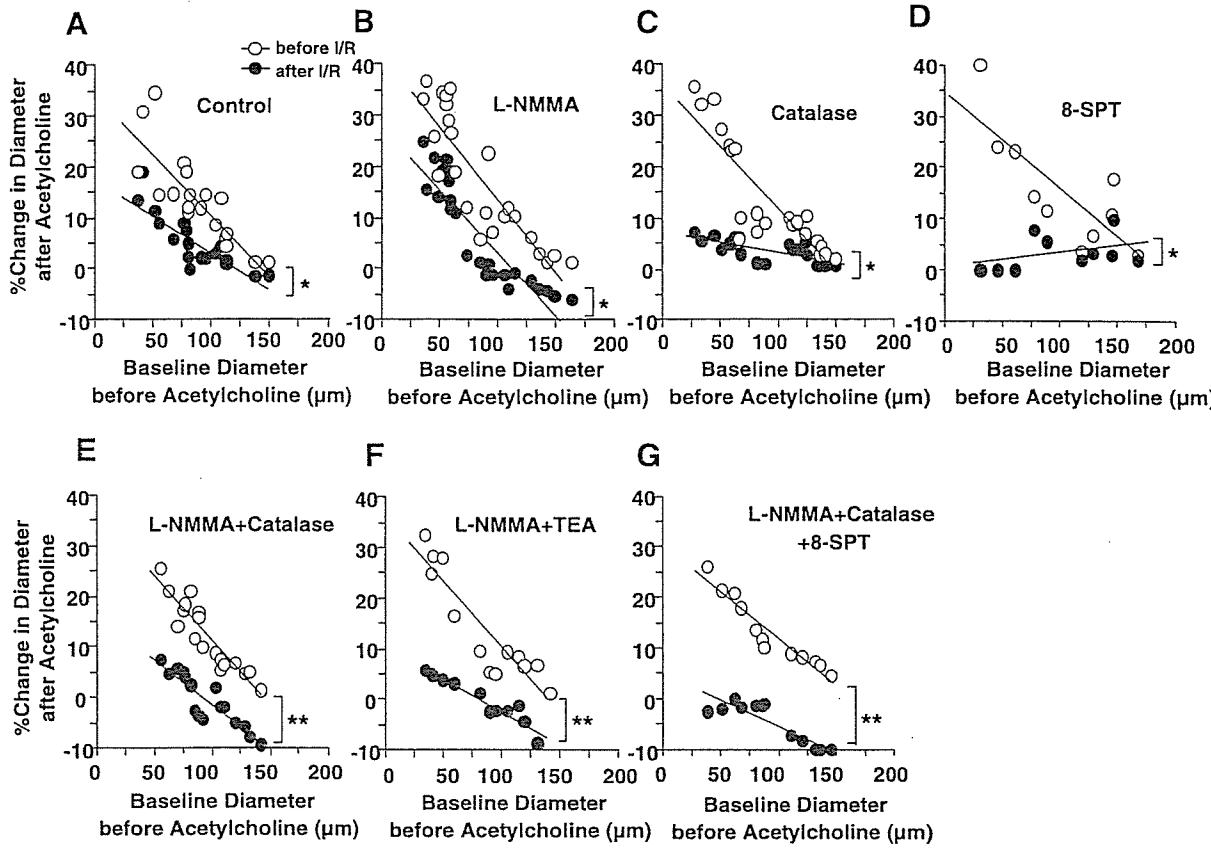

Fig. 4. Percent change in diameter after ACh before and after coronary I/R injury in dogs in vivo. No. of small arteries and arterioles per animals used was 7/5 for control (*A*), 8/5 for L-NMMA (*B*), 10/5 for catalase (*C*), 6/5 for 8-SPT (*D*), 8/5 for L-NMMA plus catalase (*E*), 5/5 for L-NMMA plus TEA (*F*), and 5/5 for L-NMMA plus catalase plus 8-SPT in small arteries (*G*); and 12/5 for control (*A*), 16/5 for L-NMMA (*B*), 12/5 for catalase (*C*), 5/5 for 8-SPT (*D*), 10/5 for L-NMMA plus catalase (*E*), 8/5 for L-NMMA plus TEA (*F*), and 7/5 for L-NMMA plus catalase plus 8-SPT in arterioles (*G*). $^*P < 0.05$, $^{**}P < 0.01$.

the infarct size (Fig. 9*A*). In the control group, there was an inverse relation between the infarct size and transmural collateral blood flow measured by microsphere technique ($r = 0.90$, $P < 0.01$). There was no significant difference in the relationship among the control, L-NMMA, and catalase treatment (Fig. 9*B*). L-NMMA plus catalase or TEA significantly shifted the regression line upward compared with the control group (both $P < 0.01$), and L-NMMA plus catalase with 8-SPT further shifted the regression line upward compared with L-NMMA plus catalase or TEA (Fig. 9*B*, both $P < 0.01$).

DISCUSSION

The major finding of the present study is that endogenous H_2O_2, in cooperation with NO, plays an important cardioprotective role during coronary I/R injury as a compensatory mechanism for NO in vivo. To the best of our knowledge, this is the first report that demonstrates the important protective role of endogenous H_2O_2, in cooperation with NO, against coronary I/R injury in vivo.

Validations of experimental model and methodology. On the basis of the previous reports (22, 31), we chose the adequate dose of ACh, SNP, L-NMMA, catalase, TEA, and 8-SPT to examine the effects of endothelium-dependent and -independent coronary vasodilator responses and inhibition of NO synthesis, H_2O_2, K_{Ca} channels, and adenosine receptor, respectively. In addition, on the basis of previous studies and our own (31, 35), we choose the doses of ACh and SNP that cause maximal coronary vasodilatation in dogs in vivo. TEA at low doses is fairly specific for K_{Ca} channel, but at higher doses it may block a number of other K channels. Because several K_{Ca} channels are involved in H_2O_2-mediated responses (26), we selected the nonselective K_{Ca} inhibitor TEA to inhibit all K_{Ca} channels (15). We have previously confirmed the validity of the methods that we used in the present study (32). After 60–90 min of ischemia, ultrastructural damage of coronary endothelium was observed particularly in the subendocardium in the present study, a finding consistent with the previous study (8).

H_2O_2 during coronary I/R in vivo. It was previously reported that relaxations of isolated large canine coronary arteries to exogenous H_2O_2 were partially endothelium dependent (23). Recently, Matoba et al. (16, 17) identified that endothelium-derived H_2O_2 is an EDHF in mouse and human mesenteric microvessels. Subsequently, we (35) and others (19) have confirmed that endogenous H_2O_2 exerts important vasodilator effects in canine coronary microcirculation in vivo and in isolated human coronary microvessels, respectively. It is conceivable that H_2O_2 is produced from superoxide anions derived from several sources in endothelial cells, including eNOS, cyclooxygenase, lipoxygenase, cytochrome *P*-450 enzymes, and NAD(P)H oxidases (16). In the present study, L-NMMA or catalase alone did not com-

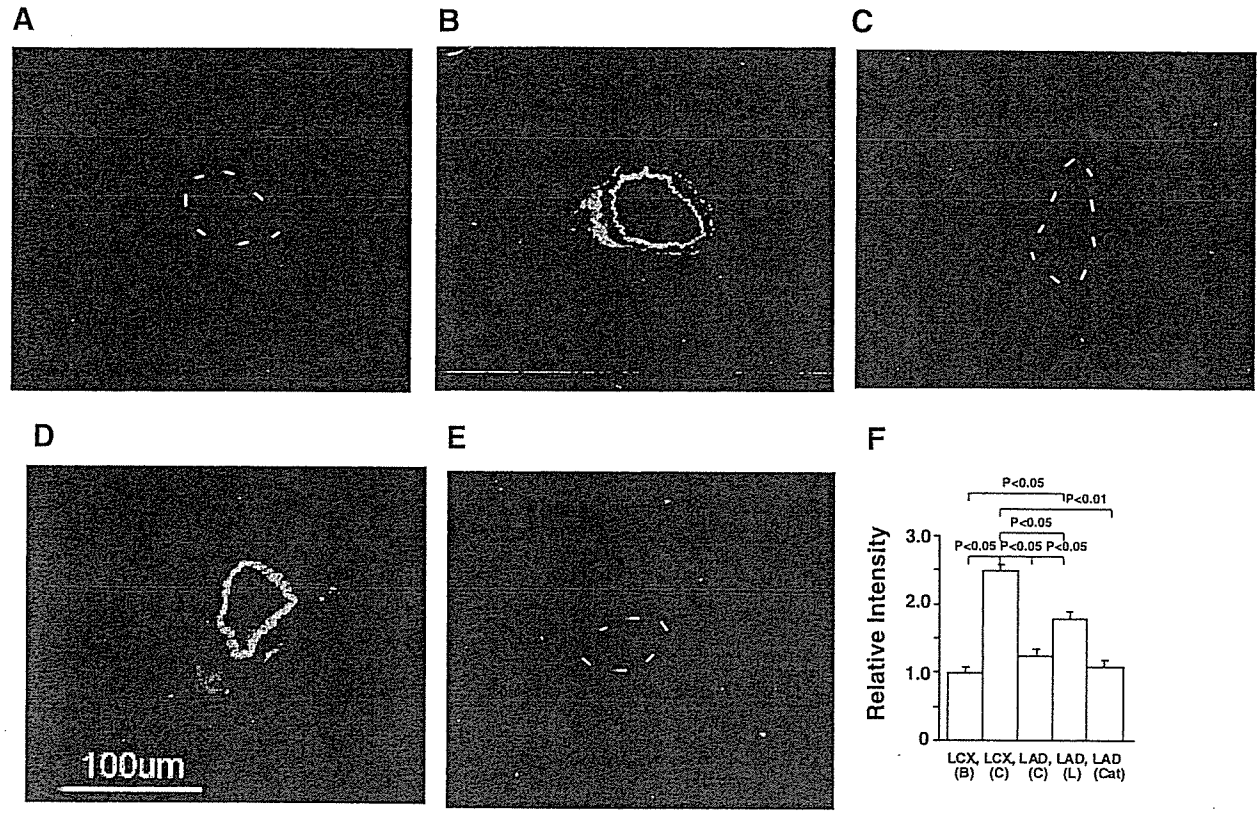

Fig. 5. Detection of H_2O_2 production. *A*: left circumflex artery (LCX; baseline without ACh). *B*: LCX (control). *C*: left anterior descending coronary artery (LAD; control). *D*: LAD (L-NMMA). *E*: LAD (catalase). *F*: fluorescent intensity (B, baseline without ACh; C, control, L, L-NMMA; Cat, catalase). No. of arterioles per animals used was 5/5 for each group. Dashed line, outline of vessels. Bar, 100 μm.

pletely abolish the ACh-induced vasodilatation in both sized arteries, whereas L-NMMA plus catalase markedly attenuated the residual vasodilatation in vivo as did TEA, indicating that H_2O_2 exerts important vasodilator effects during I/R injury in canine coronary microcirculation in vivo (Figs. 3 and 4). Furthermore, in the present study, endogenous H_2O_2-mediated coronary vasodilatation was noted to a greater extent in arterioles than in small arteries (Figs. 3 and 4), confirming the predominant role of H_2O_2 in microvessels and that of NO in relatively large arteries in vivo (25).

Compensatory vasodilator mechanism among H_2O_2, NO, and adenosine. It is well known that coronary vascular tone is regulated by the interactions among several endogenous vasodilators, including NO, H_2O_2, and adenosine (33). These vasodilators play an important role in compensatory vasodilatation of coronary microvessels during myocardial ischemia (35). In the present study (Figs. 3 and 4), endothelium-dependent arteriolar vasodilatation to ACh during coronary I/R was significantly increased by L-NMMA while small arterial vasodilatation to ACh was increased by catalase and 8-SPT, and the residual arteriolar dilation was further inhibited by both of them (L-NMMA plus catalase or TEA). Furthermore, fluorescent microscopy with DCF and DAR, respectively, showed that H_2O_2 and NO production after I/R were enhanced in small coronary arteries and arterioles by L-NMMA [fluorescent intensity (FI) 1.8] and catalase (FI 1.9) compared with those in the LAD of control group (Figs. 5 and 6, FI: DAR 1.2 and DCF 1.1). The residual small arteriolar dilatation after combined administration of L-NMMA + catalase was completely blocked by 8-SPT, an adenosine receptor blocker, indicating that adenosine also compensated for the loss of action of NO and H_2O_2. Taken together, these results indicate the compensatory vasodilator effects among NO, H_2O_2, and adenosine to maintain coronary blood flow during coronary I/R injury in vivo. H_2O_2 and NO were mutually compensatory in both small arteries and arterioles, and in the presence of their inhibitors (catalase and L-NMMA), adenosine also caused arteriolar vasodilatation, as we reported previously (35). This finding is consistent with our finding that NO, H_2O_2, and adenosine play an important compensatory role in coronary autoregulation in canine coronary microcirculation in vivo (35). It was reported that TEA inhibited adenosine-induced vasodilatation of canine subepicardial coronary arteries in vitro (3). Furthermore, H_2O_2 stimulates protein kinase C, phospholipase A_2, and arachidonic acid release and increases intracellular cAMP levels (10). These findings suggest that cAMP-mediated pathway is involved, at least in part, during coronary vasodilatation through K_{Ca} channels after I/R injury.

Role of H_2O_2 during coronary I/R. It is known that K_{Ca} channels substantially contribute to coronary vasodilatation in myocardial ischemia (22) and that H_2O_2 also activates K_{Ca} channels (11). However, it remains to be examined whether H_2O_2 contributes to coronary vasodilatation during I/R in vivo. The present results demonstrate that H_2O_2

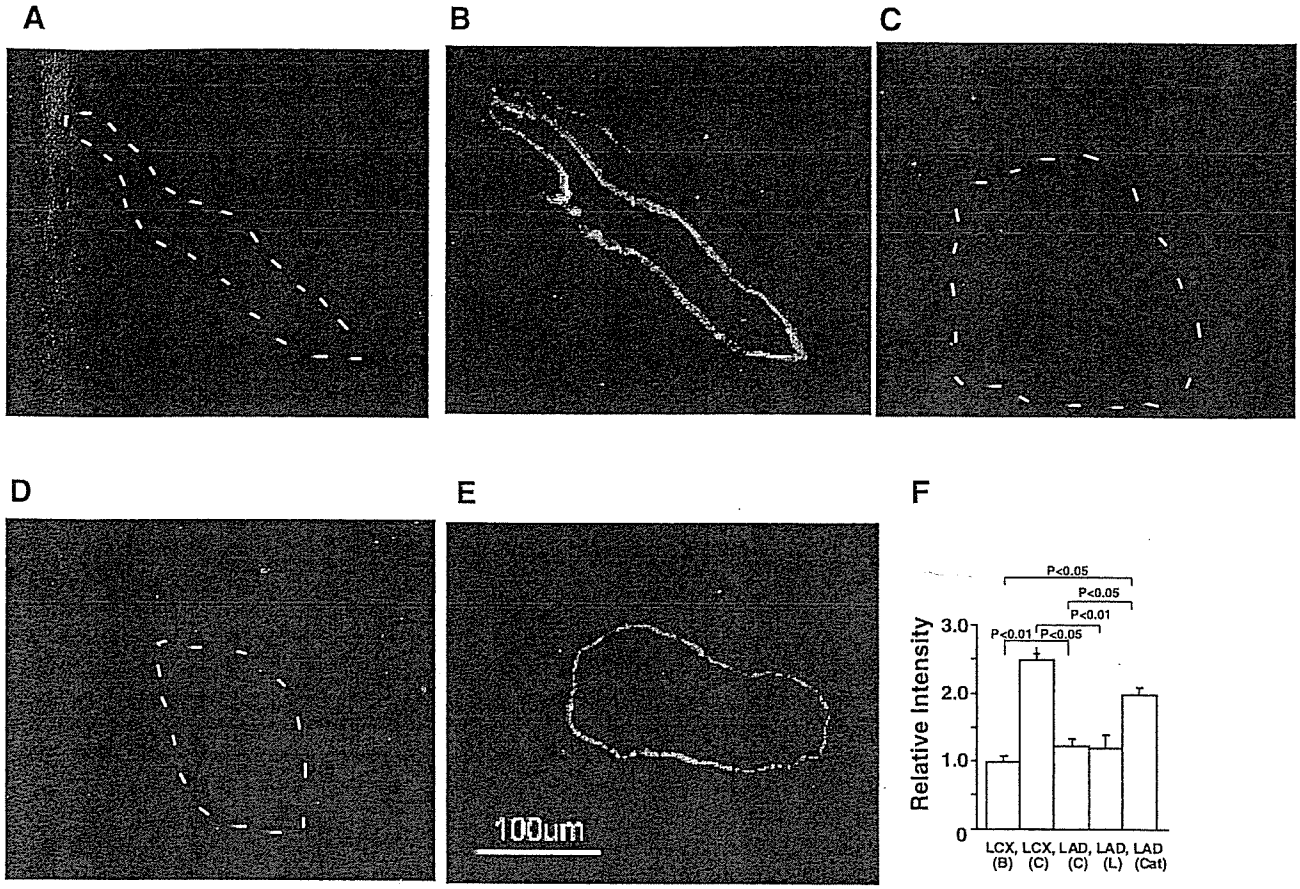

Fig. 6. Detection of nitric oxide (NO) production. *A*: LCX (baseline without ACh). *B*: LCX (control). *C*: LAD (control). *D*: LAD (L-NMMA). *E*: LAD (catalase). *F*: fluorescent intensity (B, baseline without ACh; C, control, L, L-NMMA; Cat, catalase). No. of small arteries per animals used was 5/5 for each group. Dashed line, outline of vessels.

substantially contributes to coronary vasodilatation during I/R in vivo as a compensatory mechanism for the loss of NO. Several mechanisms have been proposed for K_{Ca} channel opening during coronary I/R, including cellular acidosis

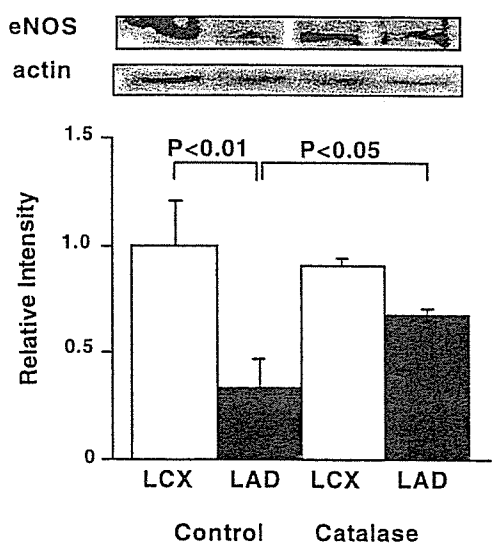

Fig. 7. Western blotting showing the effects of catalase on endothelial nitric oxide synthase (eNOS) protein expression in the myocardium of LAD and LCX. No. of animals used was 3 for each group.

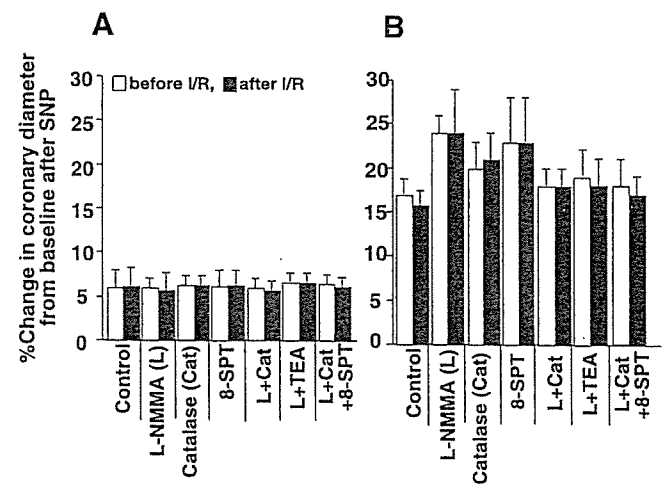

Fig. 8. Endothelium-independent coronary vasodilatation before and after coronary I/R injury in dogs in vivo. *A*: small artery (≅100 μm). *B*: arteriole (<100 μm). No. of small arteries and arterioles per animals used (*n*/*n*) was 7/5 for control, 8/5 for L-NMMA, 10/5 for catalase, 6/5 for 8-SPT, 8/5 for L-NMMA plus catalase, 5/5 for L-NMMA plus TEA, and 5/5 for L-NMMA plus catalase plus 8-SPT in small arteries; and 12/5 for control, 16/5 for L-NMMA, 12/5 for catalase, 5/5 for 8-SPT, 10/5 for L-NMMA plus catalase, 8/5 for L-NMMA plus TEA, and 7/5 for L-NMMA plus catalase plus 8-SPT in arterioles.